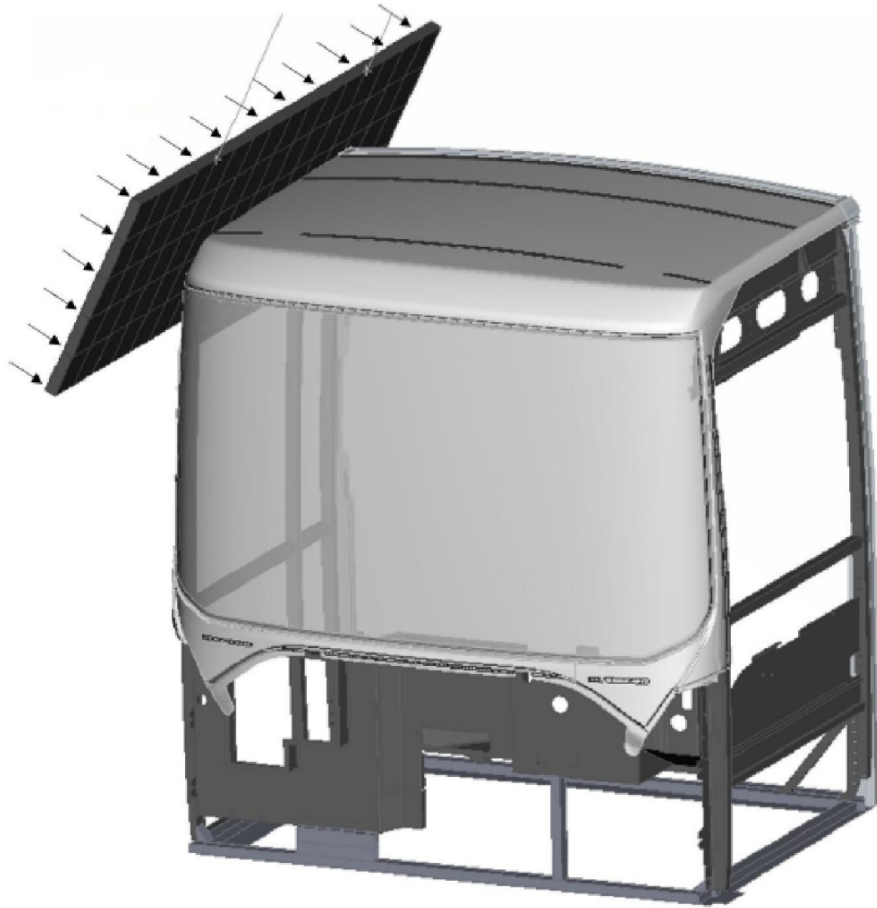




CHALMERS
UNIVERSITY OF TECHNOLOGY



Modelling of glass fibre reinforced plastic for crash applications

Master's thesis report

CHIRAG GURUMURTHY
JUEYI FANG

MASTER'S THESIS 2020

Modelling of glass fiber reinforced plastic for crash applications

CHIRAG GURUMURTHY
JUEYI FANG



Department of Industrial and Materials Science
CHALMERS UNIVERSITY OF TECHNOLOGY
Gothenburg, Sweden 2020

Modelling of glass fiber reinforced plastic for crash applications
CHIRAG GURUMURTHY
JUEYI FANG

© CHIRAG GURUMURTHY, JUEYI FANG 2020.

Supervisor: Sofie Wistrand, Volvo Bus Corporation
Examiner: Martin Fagerström, Industrial and Materials Science

Master's Thesis 2020
Department of Industrial and Materials Science
Chalmers University of Technology
SE-412 96 Gothenburg
Telephone +46 31 772 1000

Cover: The load case of the pendulum test where a pendulum hits the bus front module on its upper corner. [1]

Typeset in L^AT_EX
Printed by Chalmers Reproservice
Gothenburg, Sweden 2020

Modelling of glass fibre reinforced plastic for crash applications
Master's thesis in Applied Mechanics and Materials Engineering
CHIRAG GURUMURTHY

JUEYI FANG

Department of Industrial and Materials Science
Chalmers University of Technology

Abstract

As every automotive industry is shifting towards lightweight design, composite has become a dominant material due to its high strength to weight ratio. However, a good way of modelling composite materials needs to be investigated to facilitate for the further implementation of composite structures in future designs that are crashable. Several composites demonstrate good energy absorption character during crash e.g. bus roll over, which is beneficial, as this contributes to a steady deceleration of the impacting body. That is what makes it important to use composites for crash applications.

It is complex to understand the behaviour of composites under crash condition. Crushing of composite materials is a result of a combination of several failure mechanisms such as matrix cracking, fibre debonding, fibre fracture etc.. As technology has evolved over the years, it is now possible to mimic these failure mechanisms using commercial FE solvers. A majority of software for reinforced polymers uses various failure techniques and material models, so different approaches need to be analysed.

This study aims to simulate the mechanical behaviour of glass-fibre reinforced composite with the suitable material model available in LS-DYNA and optimise it further to use them in the crash simulation of buses.

Virtual simulations were performed with commercial Finite Element (FE) solver LS-DYNA. The mechanical behaviour of two material models (**MAT_058* and **MAT_124*) for characterising the glass fibres have been examined. Virtual simulation test results were compared to a physical coupon test results. After a detailed analysis, calibrated **MAT_058* material model was in good agreement with the experimental data compared to **MAT_124*.

Keywords: Finite Element Method, Chopped Strand Mat, crash, LS-DYNA, **MAT_058*, **MAT_124*, Ls-Opt.

Acknowledgement

The research was performed at *Volvo Bus Corporation (VBC)* in Gothenburg, Sweden. So we would like to show our gratitude and respect to our colleagues at *VBC* who constantly supported us during the tough pandemic period, without there support this project would not have been possible.

First of all we would like to thank **Sofie Wistrand** for giving us the opportunity and supervising this Master's thesis at *VBC*. Furthermore, our examiner **Martin Fagerström** deserves a huge thanks for his support, patience and guidance throughout the project. We would also like to thank **Mats Landervik**, **Torbjörn Johansen** and **David Aspenberg** from *DYNAmore Nordic* for there support in establishing the LS-DYNA and Ls-Opt modeling capabilities throughout this thesis. Lastly, we would like to thank our families and friends for their constant support, devotion and encouragement!

Chirag Gurumurthy and Jueyi Fang

Gothenburg, November, 2020

Contents

List of Figures	x
List of Tables	xii
Acronyms	xiv
1 Introduction	2
1.1 Background	2
1.2 Objectives	2
1.3 Limitation of the work	3
2 Theory	4
2.1 Composites	4
2.1.1 Fibre Reinforced Polymer	4
2.1.2 Glass fibre Reinforced Polymer (GFRP)	7
2.1.2.1 Chopped Strand Mat	8
2.2 Failure modes in composites	9
2.2.1 Matrix cracking	10
2.2.2 Matrix-fibre debonding	10
2.2.3 Fibre breakage	10
2.2.4 Fibre pull-out	11
2.3 LS-DYNA	11
2.3.1 Material Model 58: Laminated Composite Fabric	12
2.3.1.1 Description of Material Card <i>*MAT_058</i>	13
2.3.2 Material Model 124: Tension-Compression Plasticity	17
2.3.2.1 Description of material card <i>*MAT_124</i>	17
2.3.3 <i>*MAT_ADD_EROSION</i> material card	18
2.3.3.1 <i>GISSMO</i> damage model	19
2.3.3.2 Description of the material card <i>*MAT_ADD_EROSION</i>	20
2.3.4 Elements	21
2.4 Optimisation	22
2.4.1 Ls-Opt	22
3 Coupon testings	24
3.1 Tested material	24
3.2 Tensile testing	24
3.3 Compression testing	25

3.4	In-plane shear testing	26
3.5	Four-point bending testings	27
3.6	Density measurement	28
3.7	Results of coupon testings	28
4	Methodology	31
4.1	Assumptions and limitations	31
4.2	Selection of material models in LS-DYNA	31
4.3	FE Model setup in LS-DYNA	32
4.4	Implementation of <i>*MAT_058</i>	32
4.4.1	Numerical models setup	33
4.4.2	Classification of variables	36
4.4.3	<i>*MAT_058</i> baseline model	37
4.4.4	optimisation of <i>*MAT_058</i> in Ls-Opt	39
4.5	Implementation of <i>*MAT_124</i>	41
4.5.1	<i>*MAT_124</i> baseline model	45
4.5.2	Optimisation of <i>*MAT_124</i>	48
4.5.3	Implementation of <i>*MAT_ADD_EROSION</i>	48
4.5.4	Optimisation of <i>*MAT_ADD_EROSION</i>	52
5	Optimisation result and discussion	53
5.1	Calibration results of <i>*MAT_058</i>	53
5.1.1	Tension test simulation	53
5.1.2	Compression test simulation	54
5.1.3	In-plane shear test simulation	55
5.1.4	Flexural test simulation	56
5.2	Calibration results of <i>*MAT_124</i>	57
5.2.1	Tension test simulation	57
5.2.2	Compression test simulation	58
5.2.3	Shear test simulation	59
5.2.4	Flexural test simulation	60
6	Conclusion and Future work	63
6.1	Concluding remarks	63
6.2	Future work	63

List of Figures

2.1	Local co-ordinate for a single lamina.	5
2.2	Global co-ordinate system.	5
2.3	Failure modes of CSM material captured in Scanning Electron Microscope (courtesy to <i>M. Johar</i> [13]).	10
2.4	Cross-sectional area of the specimen.	12
2.5	Typical stress-strain relation of uniaxial (a) tension and (b) compression in <i>*MAT_058</i> [22].	14
2.6	Shear stress-strain diagram in MAT58 (FS=-1)[22][21].	16
2.7	von Mises yield surface in 3-D stress space for (a) <i>*MAT_024</i> [24] and (b) <i>*MAT_124</i> [25].	17
2.8	The SRSM optimisation process [courtesy to DYNAmore Nordic Training on Ls-Opt].	23
3.1	Dimension of the tensile test specimen(ISO 8256 type3 [35] tensile bar).	25
3.2	Dimension of the compression test specimen.	25
3.3	Geometry of Iosipescu in-plane shear test specimen (unit: mm) [38].	26
3.4	Schematic of Iosipescu shear fixture [37].	26
3.5	Engineering stress-strain curves of coupon testings.	30
	(a) Tensile test result	30
	(b) Compression test result	30
	(c) Shear test result	30
	(d) Flexural test result	30
4.1	(a) Tensile test model (b) Compression test model. Boundary conditions are applied on edges A and B.	34
4.2	(a) Shear test model (b) Flexural test model. Boundary conditions are applied on: edges A, B and F; points C and E and rigid parts D and G.	34
4.3	Load curve (curve ID: 4002) input for Young's modulus EA and EB.	38
4.4	Load curve (curve ID: 7001) input for in-plane shear modulus GAB.	39
4.5	Schematic flowchart of Ls-Opt.	40
4.6	An example of Ls-Opt for optimising shear-related variables in <i>*MAT_058</i>	40
4.7	Models of (a) tensile test specimen and (b) compression test specimen.	42
4.8	Shear test specimen.	43
4.9	Flexural test specimen.	44
4.10	Effective true stress vs Effective true plastic strain in tension (LCIDT).	46

4.11	Effective true stress vs Effective true plastic strain in compression (LCIDC).	47
4.12	Yield stress vs Strain rate (LCSRT).	47
4.13	optimisation process using SRSM strategy.	48
4.14	Failure strain vs triaxiality curve before optimisation (LCSDG). . . .	50
4.15	Critical strain vs triaxiality curve before optimisation (ECRIT). . . .	51
4.16	Stress vs strain values for different set of <i>DMGEXP</i> and <i>FADEXP</i> values.	51
4.17	Scale factor vs Element size curve.	52
5.1	(a) Tensile test simulation results using <i>*MAT_058</i> (b) a constant value as input for Young's modulus EA.	54
5.2	(a) Compression test simulation results using <i>*MAT_058</i> (b) a constant value as input for Young's modulus EA.	54
5.3	(a) Shear test simulation results using <i>*MAT_058</i> (b) a constant value as input for shear modulus GAB.	55
5.4	Flexural test simulation results using <i>*MAT_058</i>	56
5.5	Tensile test simulation results using <i>*MAT_124</i> and GISSMO.	57
5.6	Compression test simulation results using <i>*MAT_124</i> and GISSMO. . . .	58
5.7	Shear test simulation results using <i>*MAT_124</i> and GISSMO.	59
5.8	Flexural test simulation results using <i>*MAT_124</i> and GISSMO. . . .	60
5.9	Critical strain vs triaxiality curve after optimisation (ECRIT).	61
5.10	Failure strain vs triaxiality curve after optimisation (LCSDG).	62

List of Tables

2.1	Material Card <i>*MAT_058</i>	14
2.2	Three types of failure surface in MAT58.	15
2.3	Material card <i>*MAT_124</i>	18
2.4	Description of input parameters in <i>*MAT_124</i>	18
2.5	Material card <i>*MAT_ADD_EROSION</i>	21
2.6	Description of input parameters in <i>*MAT_ADD_EROSION</i>	21
3.1	Two procedures of four-point bending test[39].	28
3.2	Measured mechanical properties of the GFRP composite.	29
4.1	Unit system in LS-DYNA.	32
4.2	Element size used in <i>*MAT_058</i> models.	33
4.3	Boundary conditions applied in the tensile test and compression model.	34
4.4	Boundary conditions applied in the shear and flexural tests models.	35
4.5	Classification of variables in <i>*MAT_058</i> and <i>*MAT_ADD_EROSION</i>	36
4.6	Input for <i>*MAT_058</i> baseline model.	37
4.7	Input for <i>*MAT_ADD_EROSION</i> of <i>*MAT_058</i> baseline model.	37
4.8	Element size used in <i>*MAT_124</i> models.	41
4.9	Boundary condition applied for tensile test case.	41
4.10	Boundary condition applied for compression test case.	42
4.11	Boundary condition applied for shear test case.	43
4.12	Boundary condition applied for flexural test case.	44
4.13	Load rate for all four test case in <i>*MAT_124</i> material card.	45
4.14	Parameters to be optimised in <i>*MAT_124</i>	45
4.15	Parameters to be optimised in <i>*MAT_ADD_EROSION</i>	49
4.16	Triaxiality value for four test case considered in this thesis work.	49
5.1	Setup and results for tension-related variables in <i>*MAT_058</i>	53
5.2	Setup and results for compression-related variables in <i>*MAT_058</i>	54
5.3	Setup and results for in-plane shear-related variables in <i>*MAT_058</i>	55
5.4	Setup and results for flexural-related variables in <i>*MAT_058</i>	56
5.5	Setup and results for tension-related variables in <i>*MAT_124</i> and <i>*MAT_ADD_EROSION</i>	57
5.6	Error calculation in tensile test simulation.	58
5.7	Setup and results for compression-related variables in <i>*MAT_124</i> and <i>*MAT_ADD_EROSION</i>	58
5.8	Error calculation in compression test simulation.	59

5.9	Setup and results for shear-related variables in <i>*MAT_ADD_EROSION</i> .	59
5.10	Error calculation in shear test simulation.	60
5.11	Setup and results for flexural-related variables in <i>*MAT_ADD_EROSION</i> .	60
5.12	Error calculation in flexural test simulation.	61
5.13	Setup and results for variables in <i>*MAT_124</i> and <i>*MAT_ADD_EROSION</i> .	61

Acronyms

ASTM	American Society for Testing and Materials
*B_P_M	*BOUNDARY_PRESCRIBED_MOTION
*B_S	*BOUNDARY_SPC
CFRP	Carbon Fibre Reinforced Plastics
CSM	Chopped Strand Mat
DIC	Digital Image correlation
DIEM	Damage Initiation and Evolution Model
ENF	End Notched Flexural
FE	Finite Element
FEM	Finite Element Method
FRP	Fibre Reinforced Plastics
GFRP	Glass Fibre Reinforced Plastics
GISSMO	Generalised Incremental Stress-State dependent damage Model
GUI	Graphical User Interface
MSE	Mean Square Error
SEM	Scanning Electron Microscope
SMC	Sheet Moulding Compound
SRSM	Successive Response Surface Method
VBC	Volvo Bus Corporation

Nomenclature

ϵ_{max}	Maximum principal strain at failure (-)
η	Triaxiality (-)
γ_i	Engineering shear strain at i^{th} data point (-)
γ_{max}	Shear strain at failure (-)
ν_{LT}	Major Poisson's ratio (-)
ν_{TL}	Minor Poisson's ratio (-)
σ_L	Local stress in longitudinal direction (MPa)
σ_T	Local stress in transverse direction (MPa)
σ_x	Global stress in longitudinal direction (MPa)
σ_y	Global stress in transverse direction (MPa)
σ_m	Mean stress (MPa)
σ_v	von Mises equivalent stress (MPa)
τ_i	shear stress at i^{th} data point (MPa)
τ_{LT}	Local shear stress (MPa)
τ_{xy}	Global shear stress (MPa)
$\epsilon_{p,loc}$	Critical strain (-)
E	Young's modulus (MPa)
E_L	Young's modulus in longitudinal direction (MPa)
E_T	Young's modulus in transverse direction (MPa)
G_{IC}	Mode I fracture toughness (N-m ⁻¹)
G_{IIC}	Mode II fracture toughness ((N-m ⁻¹))
G_{LT}	Shear modulus associated with the axes of symmetry (MPa)
L	Longitudinal direction
T	Transverse direction
T'	Out of plane direction
V_f	Volume fraction of fibre (-)
W_f	Work of fracture (kJ-m ⁻²)
z	Distance from the mid plane of a laminate to a specific lamina (mm)
ϵ_f	Equivalent plastic strain (-)
ϵ_p	Equivalent plastic strain (-)
\mathbf{T}_1	Transformation matrix
\mathbf{T}_2	Transformation matrix
\mathbf{Q}	Stiffness Matrix (MPa)
ϵ	Strain in the laminate (-)
ϵ^0	Mid plane strain (-)
\mathbf{Q}	Stiffness Matrix (MPa)
σ_{eng}	Engineering stress (MPa)

σ_{true}	Trues stress (MPa)
σ_{yc}	Yield stress in compression (MPa)
σ_{yt}	Yield stress in tension (MPa)
[A]	Extensional stiffness matrix (MPa)
[B]	Coupling stiffness matrix (MPa)
[D]	Bending stiffness matrix (MPa)
k	Plate curvature (mm)
M	Resultant moment (MPa-mm)
N	Resultant force (MPa-mm)
A_c	Area of the voids and micro cracks (mm ²)
A_e	Effective cross-sectional area (mm ²)
A	Cross-sectional area of the material (mm ²)
D	Internal damage (-)
$\dot{\epsilon}_{strain}$	strain rate in uni-axial test(-)
ϵ_{eng}	Engineering strain (-)
$\epsilon_{true,plast}$	Effective True Plastic Strain (-)
ϵ_{true}	True strain (-)
ϵ_{xy}	Shear strain (XY) (-)

1

Introduction

As every industry is striving to decrease the carbon footprint, automotive manufacturers are using composite materials to reduce the weight of vehicles which can significantly reduce CO₂ emission. Apart from being lightweight, composite materials can often absorb more energy in crash compared to metals [2].

Glass Fibre Reinforced Plastics (GFRP) materials have been widely used as a replacement for Carbon Fibre Reinforced Plastics (CFRP) where maximum performance is not a primary requirement such as door panels, boat hull, exterior panels of bus/truck etc. Yet a good orientation of reinforcements can give significantly high strength to weight ratio compared to other materials.

1.1 Background

In the previous master thesis “Simulating fracture of laminated glass windcreens undergoing large deformations” [1], a physical pendulum test on the bus front was performed and a simulation was done in LS-DYNA [3] to capture the windscreen behaviour during a rollover. It was found out that the failure behaviour of GFRP panels was beyond expectations and could not be imitated by the current model.

This project was suggested as a master thesis by Volvo Bus Corporation (VBC) as a response to this lack of strength simulation and failure prediction of the GFRP composite.

1.2 Objectives

This master’s thesis aims to develop a methodology for simulating the mechanical behaviour of the GFRP composite in LS-DYNA for crash application.

This will be done by completing the following tasks:

- Selecting suitable material cards in LS-DYNA for modelling GFRP.
- Converting relevant experimental data from the physical coupon tests report into the material cards. (The coupon tests were performed prior to this thesis started).

- Perform virtual coupon tests for tension, compression, shear and flexural test based on the physical coupon tests.
- Identify the parameters in the selected material models that affect the final result using LS-DYNA.
- Calibrate the identified parameters using Ls-Opt software to get a close correlation between virtual and physical coupon tests.

1.3 Limitation of the work

Due to the time-frame and the background of this thesis, the following limitations exist:

- The coupon tests were performed before this thesis work started by someone else and a few testing details were missing in the received test report.
- Only one type of GFRP composite from one supplier was able to be studied. So the findings might not be applicable for other GFRP composite materials.
- Only the existing material models in LS-DYNA were calibrated.
- The material models are intended to be used in the complete bus for crash application, which limits the possible element size and puts requirements on appropriate simulation speed.
- The calibration of material models was done by performing coupon test simulation.

2

Theory

2.1 Composites

High performance application such as aircraft, aerospace and super/hyper car requires lightweight components which can bear the loads at expected boundary and environmental conditions. Such structurally efficient components require materials that have high strength and stiffness per weight. Another way of increasing the structural efficiency is by optimising the geometry of the structure itself. But an efficient design process is to consider both aspects to create an optimal design.

Generally when two or more materials, that have different physical and chemical properties, are combined into a new material which is superior to the individual materials, we call it a composite. One such composite material which has been often used in the industry is Fibre Reinforced Plastics (FRP). Under FRP, fibreglass refers to a group of products made from individual glass fibres combined into a variety of forms. This thesis presents work carried on about GFRP only.

2.1.1 Fibre Reinforced Polymer

Composites are made from two main materials, they are reinforcement and matrix. Reinforcement in FRP are made from fibres such as glass, carbon, aramid fibres and natural fibres which provide maximum strength to the composite component. Matrix material is usually an epoxy, vinylester or polyester thermosetting plastic which helps to bond the fibres together and protect the fibres from external factors such as moisture and temperature. Hence FRP's are composite materials made of a polymer matrix reinforced with fibres. Man-made/synthetic fibres made from non-polymeric materials exhibit a significant increase in strength along their lengths compared to naturally occurring materials because the latter contains more flaws when compared to synthetic fibres. Small cross-sectional dimension of the fibre gives an advantage to overcome the problem of flaws in the material.

Existence of FRP materials dates back to 1930's, but the first ever production car made from fibreglass was *Glasspar G2* in 1949 [4]. Since FRP was introduced, there has been a growing usage.

Most of the composite components made from FRP consists of several laminas stacked up one on top of another. Every components are distinguished based on

the:

- Type of reinforcement (continuous or discontinuous).
- Volume and weight fraction of both reinforcement and matrix used.
- Layup angle between each lamina's.

These three factors play a major role in characterising the material property of FRP and the classification of composite materials is explained in *Bhagwan D. Agarwal et al.* [5].

The factor behind strength and stiffness of FRP materials is it's orthotropic nature. In multilayered (angle-ply) composites, strength and stiffness varies between each lamina based on the layup angle. A local co-ordinate system is used for FRP's in each lamina. Longitudinal direction of fibre is often referred to as L or 1, transverse direction as T or 2 and out of plane direction as T' or 3. The local co-ordinate system of a single lamina is illustrated in Figure 2.1

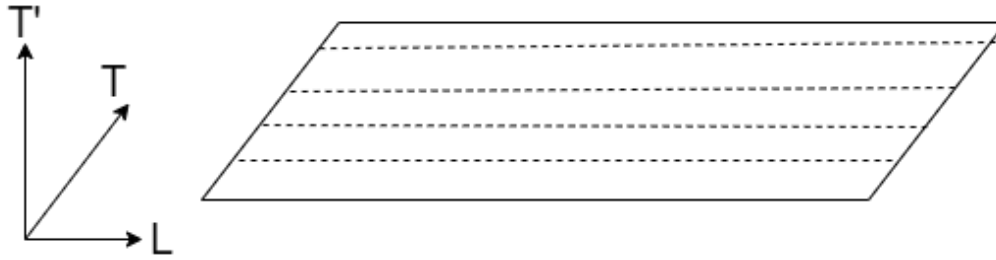


Figure 2.1: Local co-ordinate for a single lamina.

When using the lamina in a component generally a global co-ordinate system is defined to measure the strength of the laminate. According to which x is defined as longitudinal direction, y is defined as transverse direction and z is defined as out of plane direction. The angle between each lamina is determined the value of θ . The global co-ordinate system is explained in the Figure 2.2

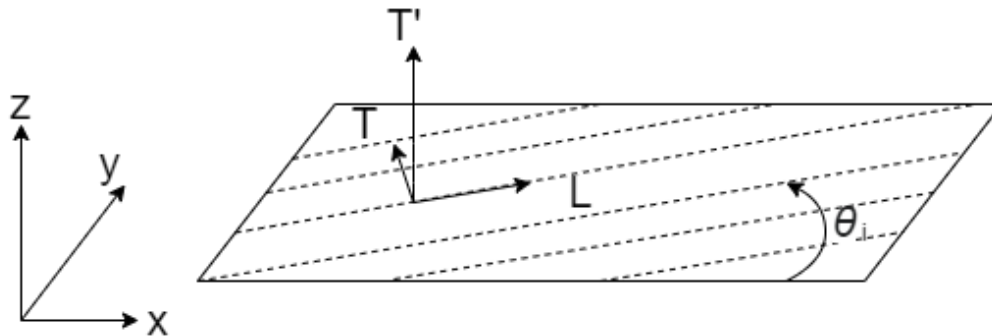


Figure 2.2: Global co-ordinate system.

The relation between material properties and stress-strain in a composite component is bridged by stiffness matrix \mathbf{Q} in Equation (2.1). In order to calculate the global stress-strain in the laminate due to applied loads, the transformation matrices \mathbf{T}_1 and \mathbf{T}_2 in Equation (2.2) and Equation (2.3) is required which will eventually help in calculating stiffness matrix $\bar{\mathbf{Q}}$ in Equation (2.4) which is similar to stiffness matrix \mathbf{Q} .

$$\mathbf{Q} = \begin{bmatrix} \frac{E_L}{1-\nu_{LT}\nu_{TL}} & \frac{\nu_{TL}E_L}{1-\nu_{LT}\nu_{TL}} & 0 \\ \frac{\nu_{LT}E_L}{1-\nu_{LT}\nu_{TL}} & \frac{E_T}{1-\nu_{LT}\nu_{TL}} & 0 \\ 0 & 0 & G_{LT} \end{bmatrix} \quad (2.1)$$

$$\mathbf{T}_1 = \begin{bmatrix} \cos^2(\theta) & \sin^2(\theta) & 2\sin(\theta)\cos(\theta) \\ \sin^2(\theta) & \cos^2(\theta) & -2\sin(\theta)\cos(\theta) \\ -\sin(\theta)\cos(\theta) & \sin(\theta)\cos(\theta) & \cos^2(\theta) - \sin^2(\theta) \end{bmatrix} \quad (2.2)$$

$$\mathbf{T}_2 = \begin{bmatrix} \cos^2(\theta) & \sin^2(\theta) & \sin(\theta)\cos(\theta) \\ \sin^2(\theta) & \cos^2(\theta) & -\sin(\theta)\cos(\theta) \\ -2\sin(\theta)\cos(\theta) & 2\sin(\theta)\cos(\theta) & \cos^2(\theta) - \sin^2(\theta) \end{bmatrix} \quad (2.3)$$

$$\bar{\mathbf{Q}} = [\mathbf{T}_1]^{-1} \mathbf{Q} [\mathbf{T}_2] \quad (2.4)$$

In a multilayered composite each lamina is orthotropic, hence it is necessary to add up the material property by the use of transformation matrix \mathbf{T}_1 , \mathbf{T}_2 and stiffness matrix $\bar{\mathbf{Q}}$ to calculate the sub matrices:

- Extensional stiffness matrix $[\mathbf{A}]$.
- Coupling stiffness matrix $[\mathbf{B}]$.
- Bending stiffness matrix $[\mathbf{D}]$.

as

$$\begin{aligned} [\mathbf{A}] &= \sum_{k=1}^k [\bar{\mathbf{Q}}]_k (h_{k-1} - h_k) \\ [\mathbf{B}] &= \frac{1}{2} \left(\sum_{k=1}^k [\bar{\mathbf{Q}}]_k (h_{k-1}^2 - h_k^2) \right) \\ [\mathbf{D}] &= \frac{1}{3} \left(\sum_{k=1}^k [\bar{\mathbf{Q}}]_k (h_{k-1}^3 - h_k^3) \right) \end{aligned} \quad (2.5)$$

Where h_k is the distance from mid-plane of laminate to the respective lamina. For the convenience of calculation it is necessary to use an equivalent system of force \mathbf{N} and moment \mathbf{M} acting on a laminate cross section. As a result, the resultant forces and moments acting on a laminate cross section are defined as follows [5].

$$\begin{bmatrix} \mathbf{N} \\ \mathbf{M} \end{bmatrix} = \begin{bmatrix} \mathbf{A} & \mathbf{B} \\ \mathbf{B} & \mathbf{D} \end{bmatrix} \begin{bmatrix} \boldsymbol{\epsilon}^0 \\ \mathbf{k} \end{bmatrix} \quad (2.6)$$

After the computation of mid-plane strain $\boldsymbol{\epsilon}^0$ and curvature \mathbf{k} from Equation (2.6), it is possible to compute the strain in each lamina as

$$[\boldsymbol{\epsilon}]_k = [\boldsymbol{\epsilon}^0] + z[\mathbf{k}] \quad (2.7)$$

with z being the distance from the mid plane to the specific lamina, an index k for now on to mark lamina specific terms.

The stress in each lamina can then be derived in global coordinates using Equation (2.7) and (2.4) as

$$\begin{bmatrix} \sigma_x \\ \sigma_y \\ \tau_{xy} \end{bmatrix}_k = [\bar{\mathbf{Q}}]_k [\boldsymbol{\epsilon}]_k \quad (2.8)$$

and then finally in local coordinates as

$$\begin{bmatrix} \sigma_L \\ \sigma_T \\ \tau_{LT} \end{bmatrix}_k = [\mathbf{T}_1]_k \begin{bmatrix} \sigma_x \\ \sigma_y \\ \tau_{xy} \end{bmatrix}_k \quad (2.9)$$

2.1.2 Glass fibre Reinforced Polymer (GFRP)

The concept of fibreglass or glass wool was patented in 1937 by *Games Slayter* [6]. Ever since it's introduction, GFRP has played a important role in composite components. It is possible to get high mechanical properties of composites, with suitable fibre orientation angle, fibre-matrix ratio and interface bonding between the fibre and matrix, to enable stress transfer. These properties make the functional characteristics of GFRP equal to steel and the specific gravity was one-quarter of the steel [7].

There are several categories under GFRP which help to enhance different mechanical properties of the composite components such as continuous fibre, discontinuous fibre and Chopped Strand Mat (CSM). This thesis focuses on CSM and following section will provide further details on CSM.

2.1.2.1 Chopped Strand Mat

In general, when reinforcement is surrounded with matrix a composite component is formed to provide the required strength and durability in a given area of operation. CSM is one of the most popular commercial E-type glass fibre products, because of its low density and strong compatibility with most polymer matrices, it is used commonly as a reinforcement material in automotive industry.

E-Glass fibre is popular in industries for its strength and electrical resistance. They are manufactured using aluminium boron silicate glass with less than 1% presence of alkali oxide materials such as aluminium oxide.

It is manufactured by chopping long glass fibres into discontinuous fibres which have a length range between 2 – 10 cm and then they are randomly oriented to provide excellent strand integrity, good wettability, dispersion, and display isotropic property all directions. Compared to unidirectional and weave glass fibres, CSM is less expensive [8].

To study the affect of load rate in the fracture of CSM a research was conducted by *Cantwell et al.*, [9]. By carrying out controlled fracture tests over a wide range of loading speeds, the rate sensitivity in CSM was assessed. Their experiment has provided an evidence that work of fracture (W_f) rises at increased loading speed and also an increase in the stored elastic energy. Such rise is thought to be correlated with the rate dependent fracture characteristics of the glass fibres.

To measure the mechanical properties of CSM for varying glass fibre content a research work was carried by *Suhas et. al.*, [10]. Three different weight fractions (15%, 30%, 45%) of E-glass CSM was used for the experiment along with CNSL-epoxy polymer matrix. Tensile strength of the specimen with 45% fibre content was 53.45% higher than specimen with 15% and 11.5% higher than specimen with 30% fibre content. Similarly the flexural strength of the specimen 45% fibre content was 78.49% higher than specimen with 15% and 22.06% higher than specimen with 30% fibre content.

CSM has marked it's presence in the pressure vessel manufacturing industry for a very long time and a design code for using GFRP has been set up by *British Standard Institution* [11]. Inter-laminar failure of CSM is noticed during the burst tests conducted on pressure vessel. To study the inter-laminar failure of CSM, *British Standard Institution* has provided *BS4994:1973* standard which specifies a experimental method for the measurement of lap shear strength of laminates. *Zhang et al.* conducted a research work on the validity of the *BS4994:1973* standard by performing it both experimentally and analytically [12]. Experimental results on the lap shear strength showed that cracks were initiated from the corners of the notches and spread up to 50% of the specimen's shear length. The direction of crack was greatly influenced by the fibre alignment. Observation from analytical method provided an insight that the reason for variation in shear strength and crack in the material was due to the accumulation of large stress concentration at the corners of the notches.

Crack initiation was induced due to transverse tension force rather than shear force and this proves that *BS4994:1973* standard method is not reliable to measure shear strength in the pressure vessel. While this study also provided information regarding the fracture mechanism, redistribution of stresses in the cracked specimen.

A research work was carried on by *Johar et al.* to investigate the mode I and mode II inter-laminar fracture behaviour of CSM material [13]. They performed DCB and three-point End Notched Flexural (ENF) tests to characterise the mode I and mode II delamination respectively. Results from experimental tests showed that the ratio of fracture toughness from mode II (G_{IIC}) to mode I (G_{IC}) was the highest ($G_{IIC}/G_{IC} = 12.9$) among all the composites considered in there literature survey. The reason for the significant high value in this ratio could be the size of the damage zone which is smaller in CSM compared to long fibre materials. In this study matrix cracking, fibre debonding and fibre breakage failure mechanisms was also observed using Scanning Electron Microscope (SEM) during crack propagation. In the three-point ENF test, sliding between the layers was also observed (shear cusps).

A study to investigate the behaviour of CSM material under Charpy impact conditions for different lamination designs was conducted by *Arfin et al.*, [14]. The impact behaviour varied for different reinforcement types used and the capability of a composite is affected greatly by the reinforcement, matrix and structure types used. Fibre fracture, fibre pull out, fibre rupture and fibre debonding damage mechanism was observed before failure for each specimens with different design configurations categorised in this study. From close-up images captured during the experiment, it was observed that the overall damage under impact test is due to fibre rupture. Finally the analytical calculation of energy absorption using ABAQUS software and from experiment showed a similar result.

In the research work carried out by *Naughton et.al*, to measure the elastic properties of CSM and weaved GFRP, the general assumption of transversely isotropic was not achieved by the experiment they conducted. The Young's modulus in two perpendicular direction (in-plane) varied by 18% for CSM, while a 27% difference was observed in weaved GFRP [15].

2.2 Failure modes in composites

It is essential to learn how different failure modes occurs in a CSM when it is subjected to different loading conditions, so that the components can be designed to avoid the catastrophe. A physical model for each type of failure mode is one way to predict *when*, *where* and *how* the failure initiates in CSM. Based on the research work carried out by *M. J. Owen et al.*, [16], *M. Johar et al.*, [13] and *Vahid Monfared* [17] on failure behaviour of CSM, four failure modes were identified and they are *matrix cracking*, *fibre debonding*, *fibre breakage* and *fibre pull-out*, they are illustrated in Figure 2.3. As fibres are randomly oriented in CSM, it is quite complicated to understand which failure mode occurs first. According to the authors [17], [18] debonding is the first failure mode that has been observed in most of the

CSM materials. The following section will explain how the above mentioned failure modes will initiate in a CSM.

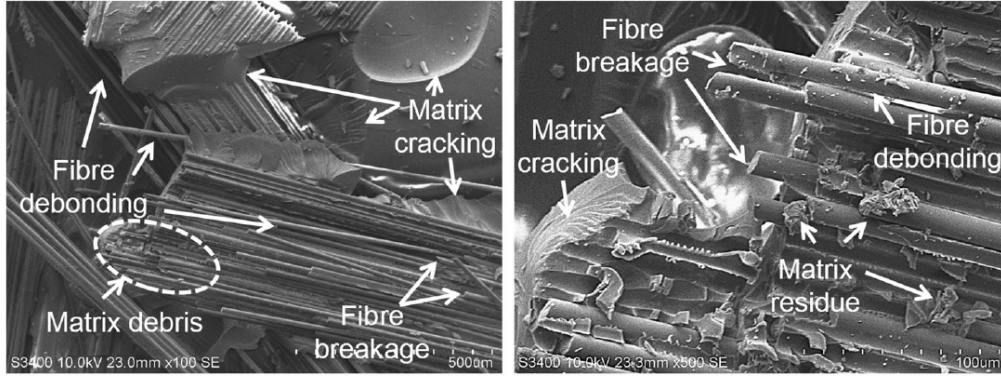


Figure 2.3: Failure modes of CSM material captured in Scanning Electron Microscope (courtesy to *M. Johar* [13]).

2.2.1 Matrix cracking

Matrix cracking in CSM is associated with cracks that form predominantly in the matrix-rich areas and are roughly perpendicular to the load direction. Matrix cracks can develop even from manufacturing defects such as pores, fibres touching. Such cracks will deviate and after reaching the fibre matrix interface, fibre debonding takes place.

2.2.2 Matrix-fibre debonding

From fracture mechanics perspective, debonding of fibre from the matrix is generally considered as an inter-facial crack. Generally, interface cracking arises in the strands which are approximately perpendicular to the load direction. But they can also occur within strands and follow the strand direction. When fibre start debonding, the cracks typically cause into more than one fibre, so that the interface crack will always grow parallel to strands.

From solid mechanics point of view, debonding is initiated when the shear stress between the fibre and the matrix exceeds the inter-facial shear strength. In this approach shear lag theory is used for the distribution of shear stress.

2.2.3 Fibre breakage

Fibre breakage in a CSM occurs When fibre reaches it's failure strain. In general, the failure strain of matrix is higher than the failure strain of reinforcement [5]. fibre breakage in a CSM under uni-axial loading case occurs in random positions. One such factor which affects the fibre fracture mode is fibre volume fraction (V_f). For instance in GFRP if $V_f < 0.4$, brittle type of failure is predominant. If V_f is the

range between 0.40 – 0.65, composite component will exhibit brittle type of failure along with fibre pullout.

2.2.4 Fibre pull-out

In a CSM material when a crack is initiated in the matrix, material (reinforcement) still has the capacity to withstand certain load and resist the crack growth. This matrix crack grows towards the reinforcement and when fibre debonds from the matrix, load carrying capacity of the fibre is further diminished. To avoid spread of fracture area after fibre reaches its failure strain, fibre is pulled out from the matrix.

2.3 LS-DYNA

Finite Element Method (FEM) approach is a well-established and convenient technology used to overcome complex mechanical problems in various engineering fields such as mechanical engineering, civil engineering, nuclear, biomedical etc.

One such commercial software developed by LSTC is LS-DYNA. LS-DYNA is a popular and powerful tool used in industries such as automotive, aerospace and biomedical. The software was initially designed to solve nonlinear dynamic transient analysis using explicit time integration method, but additional capabilities were added over the years. It can perform static, dynamic, crash, occupant safety, blast simulations. Further details about the capabilities of LS-DYNA is explained in *LS-DYNA Theory Manual* [19].

Material model:

LS-DYNA contains over 200 material models that allow for the simulation of material properties, failure initiation to evolution (damage model) and degradation schemes (failure criterion). Constitutive equations in each material model for deformation have been researched exhaustively.

Damage model and failure model:

Damage in a material may occur as voids or micro cracks when it is subjected to an increased mechanical loading as shown in Figure 2.4. After damage is initiated, material strength and material stiffness are reduced as function of damage parameters. There are two types of damage models in LS-DYNA: discontinuous damage model and continuum damage model. In a discontinuous damage model, a ply in an element is either undamaged or fully damaged and the material's elastic properties are reduced to zero once a ply fulfills failure criteria. In a continuum damage model (for example, **MAT_058*), the material softens gradually after damage initiation and then stress goes down to zero when damage equals to unity. In other words, the damaged part of the material can still withstand a certain amount of load before it is completely eroded.

Damage can be described by Equation (2.10). In which, A is the cross-sectional area of the material, A_e is the effective cross-sectional area. The effective cross-sectional area A_e can be described as $A_e = A - A_c$, in which A_c is the area of the voids and micro cracks.

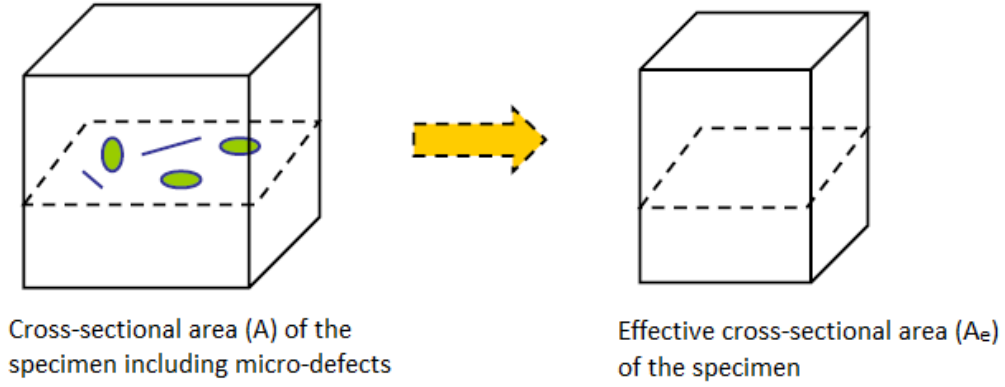


Figure 2.4: Cross-sectional area of the specimen.

$$D = \frac{A - A_e}{A} \quad (2.10)$$

When the damage D , equals to zero, it means that the material is undamaged; $D = 1$ refers to material failure and the complete loss of load carrying capacity. The values in between stand for the degree of damage.

In a failure model, final rupture will occur when a failure parameter reaches a critical value. In some cases, damage parameters can also serve as failure parameters.

2.3.1 Material Model 58: Laminated Composite Fabric

Material Model **MAT_058*, is a continuum damage model for composite laminate based on the theory developed by Matzenmiller, Lubliner and Taylor[20]. It is a material model built specifically for unidirectional composite plies and not for short fibre composites. Thereby, the failure criteria described below are not completely relevant to CSM as there is no fibre direction and no in-plane transverse direction.

**MAT_058* can be implemented for regular shell and thick shell elements to model unidirectional layers, complete laminates and woven fabrics depending on the type of failure surface. It is assumed that the irreversible micro-cracks and cavities introduced by deformation cause stiffness degradation, while the material is still able to carry load due to its remaining integrity (as long as the composite is not close to fully degradation). Once the maximum stress value is reached, the stress is reduced

according to the corresponding minimum stress limit factor.

**MAT_058* handles four failure modes and the mathematical formulations [20] of the failure criteria are considered as follows:
(based on the plane stress assumption)

- Tensile fibre mode (fibre rupture): $\sigma_{11} \geq 0$:

$$e_m^2 = \left(\frac{\sigma_{11}}{X_t}\right)^2 - 1 \begin{cases} \geq 0, & \text{failed} \\ < 0, & \text{elastic} \end{cases} \quad (2.11)$$

- Compressive fibre mode (fibre buckling and kinking): $\sigma_{11} < 0$:

$$e_c^2 = \left(\frac{\sigma_{11}}{X_c}\right)^2 - 1 \begin{cases} \geq 0, & \text{failed} \\ < 0, & \text{elastic} \end{cases} \quad (2.12)$$

- Tensile matrix mode (Matrix cracking under transverse tension and shearing): $\sigma_{22} \geq 0$:

$$e_m^2 = \left(\frac{\sigma_{22}}{Y_t}\right)^2 + \left(\frac{\tau}{S_c}\right)^2 - 1 \begin{cases} \geq 0, & \text{failed} \\ < 0, & \text{elastic} \end{cases} \quad (2.13)$$

- Compressive matrix mode (Matrix cracking under transverse compression and shearing): $\sigma_{22} < 0$:

$$e_d^2 = \left(\frac{\sigma_{22}}{Y_c}\right)^2 + \left(\frac{\tau}{S_c}\right)^2 - 1 \begin{cases} \geq 0, & \text{failed} \\ < 0, & \text{elastic} \end{cases} \quad (2.14)$$

The failure criteria above can also be interpreted as loading criteria and the yield stress acts as the threshold variables in damage model. Due to the presence of voids and micro cracks, stresses in the failure criteria should be interpreted as effective stresses [21].

2.3.1.1 Description of Material Card **MAT_058*

Input data of **MAT_058*:

Material model **MAT_058* consists of 9 cards, as shown in Table 2.1. Material property variables (blue variables) for Young's modulus, Poisson's ratio and shear modulus in different directions are mostly obtained from physical coupon tests. The damage behaviour is governed by minimum stress limit factors, $SLIM_{xx}$ (red variables), which represent the residual strength left after the damage initiation. The yellow variables in card 3, 4 and 5 control the material coordinate system. The purple variable ERODS in card 3 defines the maximum effective strain for element layer failure. In some cases, it can be set fairly high so as to disable it when it comes to element deletion. This is because a too low value might produce holes in the the model, which could lead to premature failure and unstable behaviour. The purple variable FS defines failure surface type. The green variables in card 6 and 7 control the failure initiation, which are the maximum strengths values in tension,

compression and shear and the corresponding strain values. The gray variables in card 8 and 9 are optional strain rate dependence cards, where load curves of damage initiation parameters vs. strain rate can be defined. The rest of variables were not used in this thesis.

Table 2.1: Material Card **MAT_058*.

Card 1	MID	RO	EA	EB	(EC)	PRBA	TAU1	GAMMA1
Card 2	GAB	GBC	GCA	SLIMT1	SLIMC1	SLIMT2	SLIMC2	SLIMS
Card 3	AOPT	TSIZE	ERODS	SOFT	FS	EPSF	EPSR	TSMD
Card 4	XP	YP	ZP	A1	A2	A3	PRCA	PRCB
Card 5	V1	V2	V3	D1	D2	D3	BETA	
Card 6	E11C	E11T	E22C	E22T	GMS			
Card 7	XC	XT	YC	YT	SC			
Card 8	LCXC	LCXT	LCYC	LCYT	LCSC	LCTAU	LCGAM	DT
Card 9	LCE11C	LCE11T	LCE22C	LCE22T	LCGMS	LCEFS		

Uni-axial stress-strain relation (tension and compression):

Figure 2.5 (a) illustrates a typical stress-strain relation of uniaxial tension in **MAT_058*.

The tensile stress increases initially linear elastically with the Young's modulus EA and/or EB. Then it increases nonlinearly until the maximum effective tensile strain E11T and/or E22T is reached. Once the damage is initiated, stress decreases nonlinearly to the stress decided by minimum stress limit factor, $SLIMT_x$, and the Equation (2.15). The reduced stress value is then held constant until the strain reaches the maximum effective strain, ERODS, where the layer in the element is completely removed and the material fails. Uniaxial compressive stress-strain relation is similar as that of tension, as shown in Figure 2.5 (b).

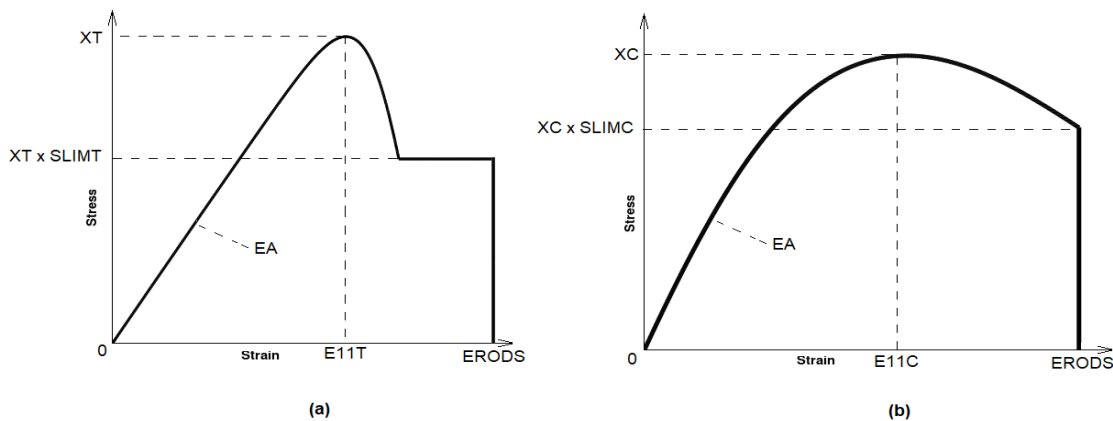


Figure 2.5: Typical stress-strain relation of uniaxial (a) tension and (b) compression in **MAT_058* [22].

The nonlinear pre-peak and post-peak response is defined by LS-DYNA based on the Matzenmiller-Lubliner-Taylor theory [20], and the slope of the smooth curve can be changed via parameter ϵ_m (i.e. E11T, E11C, E22T, E22C) which is the strain at the peak stress. Frequently, the greater the value of ExxT, the steeper the stress decrease [23]. (Note: "T" stands for "tension" and "C" stands for compression. "11" stands for longitudinal direction and "22" stands for transverse direction.)

$$\sigma_{min} = SLIM_{xx} \times strength \quad (2.15)$$

In-plane shear stress-strain relation:

*MAT_058 provides special control of shear behaviour for fabrics reinforcement and this is done by specifying the type of failure surface, FS. There are three available options, as shown in Table 2.2.

Table 2.2: Three types of failure surface in MAT58.

Failure surface type	Description	Suggested application
FS = 1.0	Smooth failure surface with a quadratic criterion for both the longitudinal and transverse directions. The shear damage is the max value of the damage from the criterion in longitudinal and transverse directions is taken.	Complete laminates and fabrics
FS = 0.0	Smooth failure surface in the transverse direction and a limiting value in the longitudinal direction.	Only for unidirectional (UD) layered composites.
FS = -1.0	Faceted failure surface. Damage evolves independently in tension, compression, and shear for both longitudinal and transverse directions.	Complete laminates and fabrics

Both failure surfaces FS=1 and FS=-1 treat all directions in a similar fashion, which coincides with the in-plane isotropy of the CSM material. However, only FS=1 was investigated in this thesis.

Figure 2.6 illustrates the shear stress-strain relation in *MAT_058. The stress-strain curve is assumed to be almost bi-linear and it is defined by two pairs of stress-strain values, *i*) TAU1 and GAMMA1 and *ii*) SC and GMS. The origin (0, 0) is assumed. In the beginning, the shear stress is assumed to increase nonlinearly from the origin (0, 0) to the point A(GAMMA1, TAU1) based on the Equation (2.16) [21][23].

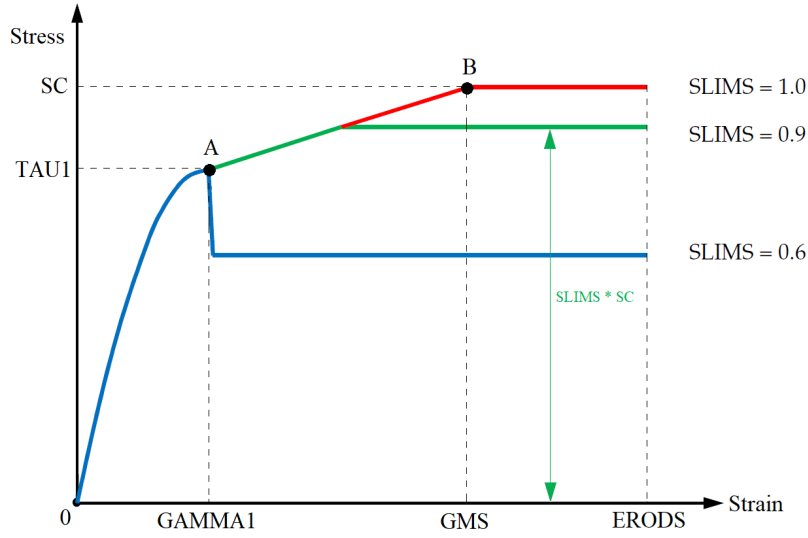


Figure 2.6: Shear stress-strain diagram in MAT58 (FS=-1)[22][21].

Then, the shear stress increases linearly to the point B(GMS, SC), where the layer is assumed to fail. Depends on the value of the shear stress limit factor (SLIMS), the stress is maintained until the maximum effective strain (ERODS) is reached.

Values for the first pair TAU1 and GAMMA1 need to be found out by optimisation tool. The second pair SC and GMS can be considered as failure stress and failure strain, which can be determined from experimental data.

Similar to the uni-axial stress-strain relation, SLIMS is used to control the post-peak response. The default value of SLIMS is 10^{-8} and a brittle failure is assumed. In order to model a more elasto-plastic behaviour for the shear part, SLIMS should be set to a larger value but not greater than 1. If SLIMS=1, as the red curve in Figure 2.6, shear stress keeps constant beyond the shear strain GMS. If SLIMS < 1, shear stress SC is never reached and the stress limit is SLIMS \times SC. For example, when SLIMS=0.9 (green curve), shear stress could only reach SC \times SLIMS; then keeps constant. For some materials, if SC \times SLIMS < TAU1 (blue curve), shear stress would first reach TAU1, then reduce to SC \times SLIMS and keep constant.

$$\sigma_i = \exp\left[-\frac{\ln\beta_i}{e}\left(\frac{E_i\epsilon_i}{\sigma_{f_i}}\right)^{\frac{1}{\ln\beta_i}}\right]\epsilon_i \cdot E_i \quad (2.16)$$

in which,

$$\beta_i = \frac{\epsilon_q}{\sigma_{f_i}} \cdot E_i \text{ and } \beta > 1$$

e is the base of the natural logarithm, σ_{f_i} is the peak stress and ϵ_q is the corresponding strain, σ_{f_i} is assumed to be identical to S_c by Schweizerhof *et. al*[21].

2.3.2 Material Model 124: Tension-Compression Plasticity

Material Model **MAT_024* in LS-DYNA is one of the prominent material model used in industry for crash simulation, drop test and other rate dependent analysis. **MAT_024* is based on von Mises theory to describe the material behaviour i.e., it follows von Mises yield surface to determine the yield condition as shown in Figure 2.7 (a).

**MAT_124* is also an isotropic elastic-plastic material model similar to **MAT_024*. The main difference between them is that the **MAT_024* material model has only one von Mises yield surface cylinder as illustrated in Figure 2.7 (a) and **MAT_124* has two von Mises yield surface cylinders as illustrated in Figure 2.7 (b). So **MAT_024* can use only one hardening curve to give relationship between stress and strain when they are in tensile or compressive mode. On the other hand **MAT_124* can use two hardening curves (one from uni-axial tension test and another uni-axial compression test) to differentiate between tension and compression behaviour in the material when they plasticise. **MAT_124* material card is useful especially when the material has different Young's modulus value in tension and compression. For further details about **MAT_124*, please refer *LS-DYNA Manual and Theory* [22],[19].

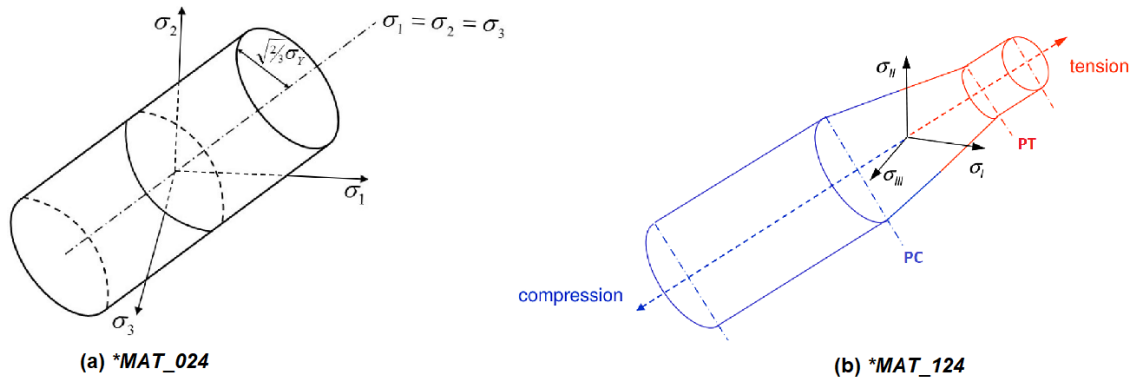


Figure 2.7: von Mises yield surface in 3-D stress space for (a) **MAT_024* [24] and (b) **MAT_124* [25].

2.3.2.1 Description of material card **MAT_124*

The variables used in **MAT_124* is shown in Table 2.3 and it consists of 5 cards. Failure of the material can be defined using this material card, variables highlighted in red are used to define failure. Variables highlighted in blue can be loaded from physical test results. To encounter the affect of strain rate, we can either use the Cowper-Symonds strain rate model or two load curves for "yield stress versus strain rate" in tension and compression can be provided using the variables highlighted in yellow. Table 2.4 provides a short description of input parameters for **MAT_124*, for detailed description please refer the LS-DYNA manual [22].

Table 2.3: Material card **MAT_124*.

Card 1	MID	RO	E	PR	C	P	FAIL	TDEL
Card 2	LCIDC	LCIDT	LCSRC	LCSRT	SRFLAG	LCFAIL	EC	RPCT
Card 3	PC	PT	PCUTC	PCUTT	PCUTF			
Card 4	K							
Card 5	G_i	BETA i						

Table 2.4: Description of input parameters in **MAT_124*.

Variable	Definition
MID	Material identification number.
RO	Mass density.
E	Young's modulus in tension.
PR	Poisson's ratio.
C, P	Strain rate parameters used in Cowper-Symonds strain rate model.
FAIL	Failure flag.
TDEL	Minimum time step size for automatic deletion of shell elements.
LCIDC	Load curve ID defining effective stress vs effective plastic strain in compression.
LCIDT	Load curve ID defining effective stress vs effective plastic strain in tension.
SRFLAG	Formulation for rate effects.
LCFAIL	Optional load curve ID defining effective plastic strain at failure vs strain rate.
EC	Young's modulus in compression.
RPCT	Fraction of PT and PC.
PC	Compressive mean stress (pressure) at which the yield stress follows load curve ID, LCIDC.
PT	Tensile mean stress (pressure) at which the yield stress follows load curve ID, LCIDT.
PCUTC	Pressure cut-off in compression (PCUTC must be greater than or equal to zero).
PCUTT	Pressure cut-off in tension (PCUTT must be greater than or equal to zero).
PCUTF	Pressure cut-off flag activation.
K	Optional bulk modulus for the viscoelastic material.
G_i	Optional shear relaxation modulus for the i^{th} term.
BETAi	Optional shear decay constant for the i^{th} term.

2.3.3 **MAT_ADD_EROSION* material card

LS-DYNA has developed several material models which inherently include failure criteria and damage formulations. For instance the composite material models **MAT022*, **MAT054*, **MAT158* are developed to capture material failure and damage within the material card.

There are several other material models such as **MAT_024* and **MAT_124* which are not developed along with a damage model, instead LS-DYNA provides the user to define failure and damage parameters using an additional keyword **MAT_ADD_EROSION*.

This keyword can also be included for constitutive models with existing failure.

Generalised Incremental Stress-State dependent damage Model (GISSMO) and *Damage Initiation and Evolution Model (DIEM)* are the two damage models which are exclusively used in **MAT_ADD_EROSION* to capture damage and failure in the material. This thesis focuses mainly on *GISSMO* damage model.

2.3.3.1 *GISSMO* damage model

One of the important input parameter for the *GISSMO* damage model is stress triaxiality (η). It is assumed that during the tensile test for isotropic material, stress is occurring in only one direction. If we consider that this isotropic material is ductile in nature, then after necking the stress will no longer be in one direction but will turn into a multi-axial stress case. This stress triaxiality value will help in determining the different stress states developed in the material during the simulation. Stress triaxiality is defined as the ratio of hydro-static stress or mean stress (σ_m), to the von Mises equivalent stress (σ_v):

$$\eta = \frac{\sigma_m}{\sigma_v} \quad (2.17)$$

with σ_m being mean stress (or first invariant of the stress tensor) for a plane stress condition (as shell elements are used for the entire thesis):

$$\sigma_m = \frac{\sigma_1 + \sigma_2}{3} \quad (2.18)$$

$$\sigma_v = \sqrt{\sigma_1^2 + \sigma_2^2 - \sigma_1\sigma_2} \quad (2.19)$$

This stress triaxiality is very important to develop the "critical strain vs triaxiality" and "failure strain vs triaxiality" curves which are used in *GISSMO* damage model.

A nonlinear form of instability measurement F in the material which couples the *GISSMO* damage model to **MAT_ADD_EROSION* material card is introduced using the Equation (2.20).

$$\Delta F = \frac{DMGEXP}{\varepsilon_{p,loc}} * F^{(1 - \frac{1}{DMGEXP})} * \Delta \varepsilon_p \quad (2.20)$$

Input data for material instability measurement are typically not available directly from coupon experiments, whereas by following reverse engineering for various stress states reasonable values are obtained. $DMGEXP$ represents the damage exponent, consider $\Delta \varepsilon_p$ as notation for equivalent plastic strain increment and ΔF represents the increment of instability measurement F for each time step. $\varepsilon_{p,loc}$ is the critical strain depending on the current triaxiality value when the material reaches instability and it is obtained from "critical strain vs triaxiality" curve.

GISSMO damage model is based on an incremental formulation of damage accumulation [19] which allows for a non-linear relation between internal damage and plastic strain:

$$\Delta D = \frac{DMGEXP * D^{(1 - \frac{1}{DMGEXP})}}{\varepsilon_f} * \Delta \varepsilon_p \quad (2.21)$$

D is the internal damage accumulated in the material and ΔD is the increment of internal damage D accumulated for each time step. Damage exponent $DMGEXP$ in Equation (2.21) contributes for non-linear accumulation of damage until failure. ε_f serves as equivalent plastic strain to failure as a function of current triaxiality value η . The internal damage accumulation equation provides the damage model a flexibility to fit material test data from, a wide range of materials in the industry. After an instability in the material has been triggered, the damage measurement D is initialised to a value of $1 * 10^{-20}$.

When the material instability measurement F in Equation (2.20) reaches unity, the damage accumulation Equation (2.21) is coupled to the stress tensor as stated in Equation (2.22).

$$\sigma^* = \sigma \left(1 - \left(\frac{D - D_{crit}}{1 - D_{crit}} \right)^{FADEXP} \right) \quad (2.22)$$

Stress tensor σ^* is accomplished by modifying the effective stress concept proposed by *Lemaitre* [26]. D_{crit} is one such parameter which is activated when $F = 1$, it can be provided as a fix value to the damage model or it can be determined from the current damage value when the material reaches instability through "critical strain vs triaxiality" curve. $FADEXP$ is element size dependent, it impacts how the material softens and the amount of energy dissipated when a element is eroded. After the material reaches instability, damage accumulation is initiated and there is a continuous reduction of stress σ^* . When damage measurement D reaches unity, the load bearing capacity of the material is vanished, so stress tensor σ^* will be equal to zero.

2.3.3.2 Description of the material card **MAT_ADD_EROSION*

**MAT_ADD_EROSION* material card consists of 7 specific cards. Table 2.5 describes the variables of the material card **MAT_ADD_EROSION*. Card 1 and 2 consists of various failure criteria that can be defined by the user, based on the mode of failure and the physical test data available. Card 3 and 4 are used for defining the *GISSMO* damage parameters while card 5 and 6 are meant for defining the *DIEM* damage parameters. Card 7 is an optional card with additional failure criteria. Table 2.6 provides a short description of input parameters for **MAT_ADD_EROSION*, for detailed description please refer the LS-DYNA manual [22].

Table 2.5: Material card **MAT_ADD_EROSION*.

Card 1	MID	EXCL	MXPRES	MNEPS	EFFEPS	VOLEPS	NUMFIP	NCS
Card 2	MNPRES	SIGP1	SIGVM	MXEPS	EPSSH	SIGTH	IMPULSE	FAILTM
Card 3	IDAM	DMGTYP	LCSDG	ECRIT	DMGEXP	DCRIT	FADEXP	LCREGD
Card 4	SIZFLG	REFSZ	NAHSV	LCSRS	SHRF	BIAXF		
Card 5	DITYP	P1	P2	P3				
Card 6	DETYP	DCTYP	Q1	Q2				
Card 7	LCFLD		EPSTHIN	ENGCRIT	RADCRT			

Table 2.6: Description of input parameters in **MAT_ADD_EROSION*.

Variable	Definition
MID	Material card identification number.
NUMFIP	Number of failed integration points prior to element deletion.
IDAM	Flag for damage model.
DMGTYP	For GISSMO damage type.
LCSDG	Load curve ID for "Effective plastic strain vs triaxiality".
ECRIT	Load curve ID for "Critical effective plastic strain vs triaxiality".
DMGEXP	Exponent for non-linear damage accumulation.
DCRIT	Damage threshold value.
FADEXP	Exponent for damage-related stress fadeout.
LCREGD	Load curve ID defining element size dependent regularization factors for equivalent plastic strain to failure in the GISSMO damage model.
SIZFLG	Flag for method of element size determination.
REFSZ	Reference element size, for which an additional output of damage will be generated.
NAHSV	Number of history variables from damage model which should be stored in standard material history array for postprocessing.
LCSRS	Load curve ID defining failure strain scaling factor for LCSDG vs strain rate.
SHRF	Reduction factor for regularisation at triaxiality=0 (shear)
BIAXF	Reduction factor for regularisation at triaxiality= 2/3 (biaxial)

2.3.4 Elements

In general, there are several Finite element types available for the user and it has to be selected based on the individual/organisation's computational budget, efficiency, required accuracy and application. *Saiphon et al.* [27] conducted a research work to analyse the performance of composite plates using shell elements in LS-DYNA for unsymmetric layups. By implementing Belytschko-Leviathan (ELFORM8) element formulation for unbalanced and unsymmetric composite layup, the anticipated coupling between membrane and bending/twisting deformations was observed. But when the number of time steps for load application became too high in symmetric layups, there was a large unexpected bending deformations observed. *Shahkarami et al.* [28] implemented shell elements for the geometric representation of the numerical model they developed to predict the impact behaviour of the composite fabric pan-

els. The FE model used for the impact analysis was efficient and correlated with the physical impact test by capturing the impact response for the composite panels used in the research work. LS-DYNA provides it's users various element formulations for four node isoparametric shell elements. Detailed element formulation is explained in LS-DYNA theory manual [19]

2.4 Optimisation

In simple words optimisation is a problem in which certain parameters (design variables) need to be determined to achieve the best measurable performance (objective function) under given constraints.

The success of LS-DYNA to better understand the physical experiments by numerical simulation has thrown a light on the development of simulation based optimisation tools such as Ls-Opt [29].

2.4.1 Ls-Opt

Ls-Opt provides users two types of optimisation, they are *Metamodel-based optimisation* and *Direct optimisation*. By utilising the results obtained from simulation only, *Direct optimisation* based method utilises genetic algorithm to find optimal results. This method is quite expensive as it requires a large number of simulations.

Metamodel-based optimisation method adapts a procedure of creating an inexpensive surrogate/meta-model of the actual design for evaluation rather than using only the simulation results. Ls-Opt provides four different strategies to solve these *Metamodel-based optimisation*:

- Single Iteration.
- Sequential.
- Sequential with Domain Reduction.
- Efficient Global optimisation.

In recent years, the most efficient optimisation method used in industry and research field is Sequential with Domain Reduction generally termed as *Successive Response Surface Method (SRSM)*. Two test cases was provided by *David et al.* [30] to demonstrate the reliability of SRSM as a tool for material identification. One test case involves the parameter identification of the power-law material model used for performing the uni-axial tensile test and determining the experimental reaction force and deformation. Another test case is associated with the identification of material model between user defined model and **MAT096* (available in LS-DYNA) for characterising the brittle damage in a composite laminated structure. For a diverse range of material laws used for non-linear material behaviour, *SRSM* strategy was clearly able to identify the material properties with fewer than 6 iterations.

Heiner et al. [31] exhibits the usage of *SRSM* optimisation strategy to determine the parameters used in a non-linear material model (**MAT083* available in LS-DYNA). Ls-Opt performed well in identifying the input parameters for a low density foam

and the simulation result showed an improved behaviour from baseline model to a optimised material model. The usage of Ls-Opt for optimising the material and failure parameters of a material model used for CFRP was presented by *Sheng et al.* [32]. In general it is very tough to get a close correlation relation between physical test result and virtual simulation test result by feeding the basic material properties obtained from coupon tests to the constitutive models. Specifically for material models such as **MAT054* and **MAT058* which are meant for laminated composites, consists of unphysical parameters such as *SLIM* values which vary in tension, compression and shear. They play an important role in capturing material behaviour in every aspect and based on the literature survey authors used by *SRSM* strategy for optimisation, an excellent set of values for the parameters used in the material model was achieved. So based on the valid research work described above, *SRSM* strategy was adapted for *Metamodel-based optimisation* in this thesis work and Figure 2.8 provides an overview of the optimisation process followed in Ls-Opt to achieve the optimum result.

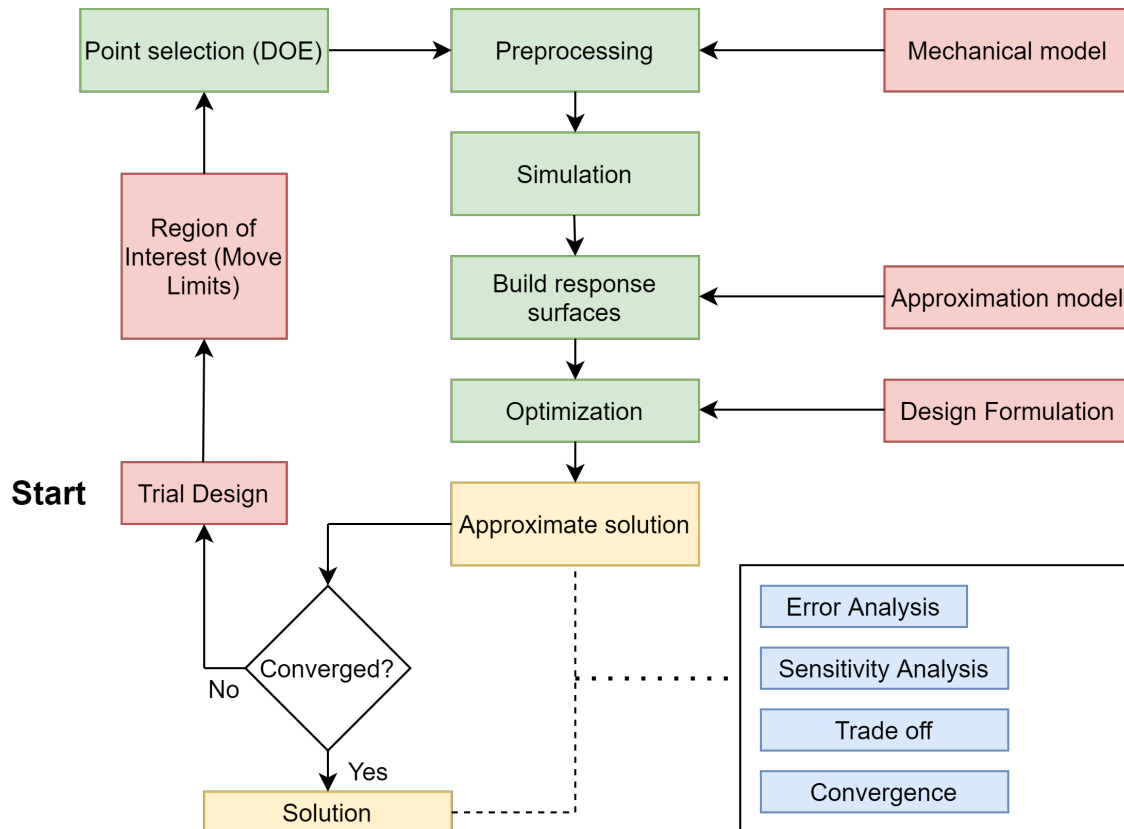


Figure 2.8: The SRSM optimisation process [courtesy to DYNAmore Nordic Training on Ls-Opt].

3

Coupon testings

This chapter presents the coupon testings that the simulation models in the later chapter were based on. All tests were performed prior to the thesis work started. The experimental data were used to compare with the simulation results.

Four types of quasi-static tests and a density measurement test were done to characterise the mechanical properties of the GFRP composite: uni-axial tensile test, uni-axial compression test, in-plane shear test, four-point flexural test.

All tests were performed at room temperature (20°C , 52% RH) and all specimens (except for samples for density measurement) were conditioned at 23°C , 50% RH for 40 hours.

3.1 Tested material

The tested material was a GFRP composite, in which a chopped strand mat made of glass fibre was used as reinforcement.

3.2 Tensile testing

Specimen geometry:

The tensile test specimens were prepared according to ISO 8256 type3 [33], the specimen dimension is as shown in Figure 3.1. The thickness t is 3.22 mm and the inner width w is 10.13 mm.

Test setup:

Tensile tests were performed as described in American Society for Testing and Materials (ASTM) D638-14 standard [34] using a servo hydraulic machine (Instron 8872) and extensometer (class B-1) was used for measuring the specimen displacement. Gauge length was 8 mm. To check if the material is strain dependent or not, tensile test was conducted for 0.01, 0.1, 1.0, 10, 100 s^{-1} strain rate values. Since it is assumed that the specimen stretches uniformly (no necking/localisation) and the strain rate is spatially uniform over the whole specimen in the uni-axial tensile test, the following equations holds good:

$$r_{strain} = \frac{r_{loading}}{L} \quad (3.1)$$

in which, L = free length of specimen between the two grips; $r_{loading}$ = loading rate.

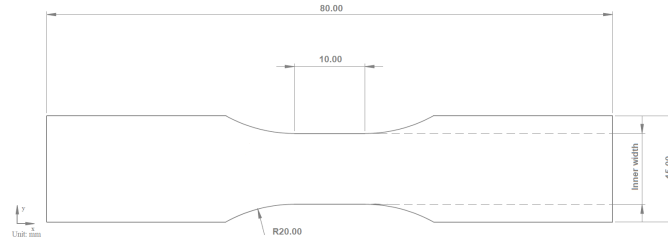


Figure 3.1: Dimension of the tensile test specimen(ISO 8256 type3 [35] tensile bar).

3.3 Compression testing

Specimen geometry:

The specimens have a rectangular geometry as shown in Figure 3.2: 140 mm long, 12.744 mm wide and 3.158 mm thick. Gauge length after clamping is 6.35 mm.

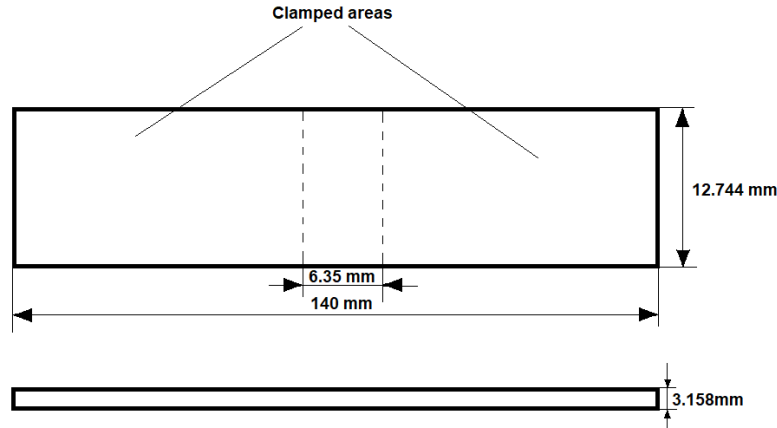


Figure 3.2: Dimension of the compression test specimen.

Test setup:

Compression tests were performed as described in ASTM D6641/D6641M-09 standard [36] on the Instron 5566 Universal Testing Machine. Specimens were clamped in a combined loading compression fixture. A constant cross-head speed 1.3 mm/min was used.

3.4 In-plane shear testing

Specimen geometry:

Shear tests were performed as described in ASTM D5379 standard [37] which is commonly known as Iosipescu shear test which was originally proposed by Iosipescu in 1967. The geometry of the tested specimen is shown in Figure 3.3.

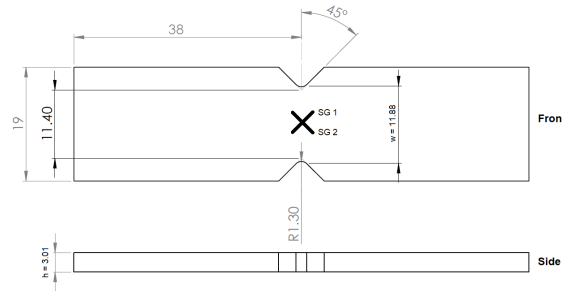


Figure 3.3: Geometry of Iosipescu in-plane shear test specimen (unit: mm) [38].

Test setup:

Shear tests were performed on a servo-hydraulic machine (Instron 8872). The specimen was loaded by a constant cross-head speed of 2 mm/min through bottom and top sides in the Iosipescu shear fixture (See Figure 3.4), which can be idealised as an asymmetric four-point bending. The small sample size with V-notches ensure a distribution of pure and uniform shear stress in the notch area. Digital image correlation (DIC) test system which consists of high-resolution cameras and an image analysis program was adopted to measure the strain field.

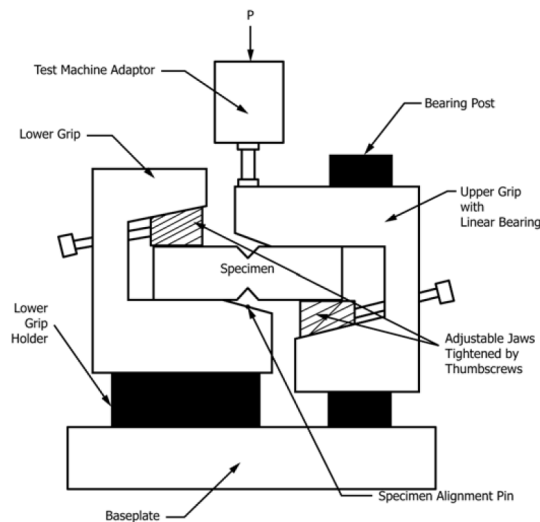


Figure 3.4: Schematic of Iosipescu shear fixture [37].

Calculation:

ASTM D5379 provides calculation of shear stress as follows:

$$\tau_i = \frac{P_i}{A} \quad (3.2)$$

where:

τ_i = shear stress at i^{th} data point, (MPa);
 P_i = the resultant loading force at i^{th} data point (N);
 A = cross-sectional area = $w \times h$ (mm²);
 w = specimen width across the notch (mm);
 h = specimen thickness at the notch (mm);

and engineering shear strain:

$$\gamma_i = |\epsilon_{+45}| + |\epsilon_{-45}| \quad (3.3)$$

where:

γ_i = engineering shear strain at i^{th} data point;
 ϵ = normal strain (also referred to shear strain tensor) at i^{th} data point, subscripts ± 45 indicating the gauge directions.

3.5 Four-point bending testings

Specimen geometry:

Flexural tests were conducted according to ASTM D6272-17 standard [39] and the specimens had a rectangular geometry with recommended dimensions as described in test standard : 127 mm long, 12.754 mm wide and 3.15 mm thick.

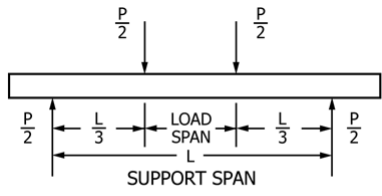
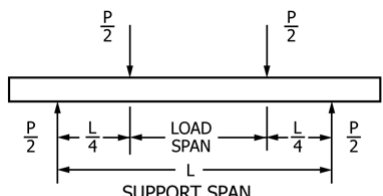
Test setup:

Testings were performed on Instron 5566 materials testing system. Test standard ASTM D6272-17 provided two testing procedures A and B [39]. Procedure A was designed for materials that break at comparatively small deflections and it is suitable for measuring flexural properties, particularly flexural modulus. Procedure B was designed for materials that undergo large deflections during testing and it is suitable for measuring flexural strength. However, the test report doesn't provide which procedure was used in the test. Loading diagram and the calculation equations for both procedures are presented in Table 3.1.

The support span L between lower supports was 50.8 mm and the test was conducted at a constant strain rate of 0.01 min^{-1} . The information about loading noses and supports are not described in the test report, but the default requirement given by ASTM D6272 standard is that both of them have cylindrical surfaces with a radii of 5 mm.

3. Coupon testings

Table 3.1: Two procedures of four-point bending test[39].

	Procedure A	Procedure B
Loading diagram	 <p>Procedure A: 1/3 Support span</p>	 <p>Procedure B: 1/2 Support span</p>
Flexural Strength (Stress in the outer fibre throughout the load span)	$S = \frac{PL}{bd^2}$	$S = \frac{3PL}{4bd^2}$
Flexural Strain	$r = \frac{Dd}{0.21L^2}$	$r = \frac{Dd}{0.23L^2}$

In which, P = load at a given point on the load-deflection curve (N);

L = support span (mm);

b = width of beam (mm);

d = thickness of beam (mm);

D = mid-span deflection (mm);

3.6 Density measurement

The solid density was measured according to ASTM D792-13 [40] (Method A). Two replicates were done and the measured average density is 1838.3 kg/m³.

3.7 Results of coupon testings

Five samplings per each type of tests were tested. One of the five curves has been selected for the material card implementation in Chapter 4.

For the implementation of **MAT_058* in Chapter 4, the samples with the weakest mechanical properties (i.e. the lowest modulus values) were chosen for a conservative safe design, which are listed as 'Selected curve A' in the Table 3.2 below.

For extrapolating the hardening curves it is good to consider a specimen which has accumulated high stress and strain. Hence for the implementation of **MAT_124* in Chapter 4, the samples with high stress and strain values from the coupon test

report was selected. The material property of the selected specimen is listed as 'Selected curve B' in the Table 3.2 below.

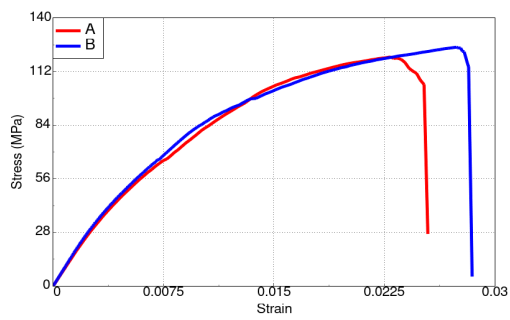
Table 3.2: Measured mechanical properties of the GFRP composite.

Test type & method		Property*		
		Modulus E, MPa	σ_{yield} , MPa	ϵ_{yield}
Tension test: ASTM D638-14	Selected curve A	11206	119.7	0.0229
	Selected curve B	11736	124.8	0.0274
	Mean value ± Std. Dev	11435±199	119.7±4.2	0.0225±0.35
Compressive test: ASTM D6641M-09	Selected curve A	9770.5	172.72	0.0343
	Selected curve B	11370.3	192.64	0.0266
	Mean value ± Std. Dev	11122±1283	180.9±13.2	0.0276±0.53
Shear test: ASTM D5379-12	Selected curve A	7421	73.1	0.0133
	Selected curve B	8183	73.6	0.01
	Mean value ± Std. Dev	7985±397	70.1±4.7	0.011±0.17
Four-point bending test: ASTM D6272-17	Selected curve A	8434.7	159.1	0.033
	Selected curve B	12790.3	251.5	0.029
	Mean value ± Std. Dev	10414±1573	198.7±34.3	0.0295±0.22

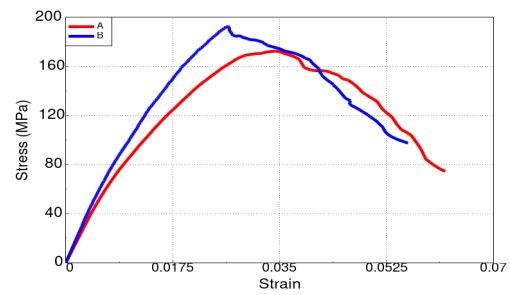
*The stress and strain are engineering values.

Engineering stress-strain curves of the above tests are shown in Figure 3.5. Curve A was used as target curve for **MAT_058*; curve B was used as target curve for **MAT_124*.

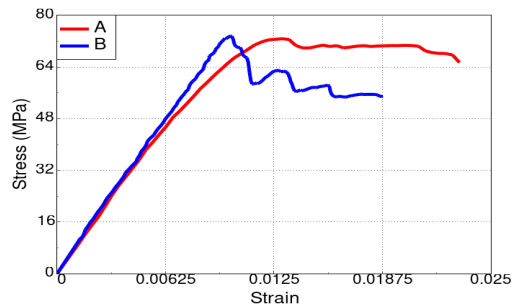
3. Coupon testings



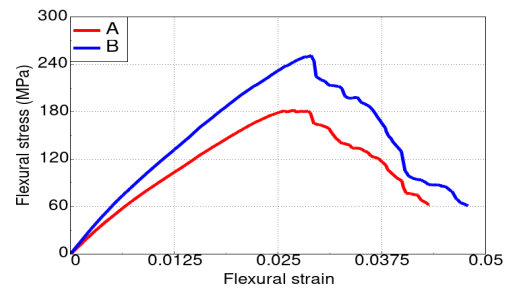
(a) Tensile test result



(b) Compression test result



(c) Shear test result



(d) Flexural test result

Figure 3.5: Engineering stress-strain curves of coupon testings.

4

Methodology

This chapter is dedicated to provide an insight about the approach followed in modeling the GFRP for crash application. It contains the assumptions, limitations and methodology adapted to achieve the end result. The implementation of the test data into the material card, boundary and loading conditions is also conferred in this chapter.

4.1 Assumptions and limitations

Based on the literature survey described in Section 2.1.2.1, we had an important assumption that CSM has in-plane isotropic property.

As explained in Section 2.3.4, shell elements prove to be efficient in capturing the physical test data. Computational time can also be reduced by implementing shell elements over solid elements. But there are certain drawbacks of using shell elements, one such issue is stress in the out of plane direction. So shell elements cannot capture stress in the direction perpendicular to the surface/plane of the shell. Shell elements is utilised to model all the test specimens in this thesis, hence plane stress condition is a limitation throughout this thesis work.

4.2 Selection of material models in LS-DYNA

There are material models available in LS-DYNA which are meant for composite materials. Since CSM falls under composite materials, initially only material models such as **MAT_054*, **MAT_055*, **MAT_058* was investigated. But composite materials are anisotropic in nature and since it was assumed that CSM has isotropic property, material models such as **MAT_24*, **MAT_123*, **MAT_124* which are extensively used for metals was investigated. Hence for this thesis work two material cards (**MAT_58* and **MAT_124*) are investigated for characterising the behaviour of CSM.

**MAT_24*, **MAT_123*, **MAT_124* material models does not inherently include failure criteria and damage formulations. Instead LS-DYNA provides the user to define failure and damage parameters using an additional keyword **MAT_ADD_EROSION*. So this is the material card where the *GISSMO* damage model is used.

4.3 FE Model setup in LS-DYNA

The entire thesis work was carried on using ANSA as preprocessor (version 19.1), LS-DYNA as FE implicit solver with single precision (version R11.1) and META as post-processor (version 20.1). LS-DYNA performs the FE analysis using a single executable file which contains geometry (node and element numbers), material data and characteristics of the model because LS-DYNA is developed as a 'command line driven software'. Predefined keywords listed in the *LS-DYNA Keyword User's Manual Volume I* [3] and *Volume II* [22] are used to model the specimen and implement features to the material card.

Unit system:

Since there is no way of specifying the units in LS-DYNA, units must be consistent [41]. Table 4.1 is the units used for all simulations in this thesis.

Table 4.1: Unit system in LS-DYNA.

Quantity	Mass	Length	Time	Force	Pressure	Velocity	Density
Unit	tonne	mm	s	N	MPa	mm/s	ton/mm ³

General settings:

All four test cases have fully integrated shell element formulation (ELFORM=16) along with 5 integration points through the thickness in *SECTION_SHELL. The matrix and reinforcement of the composite material was modeled together as one single-layer shell part. Ideally, element size of the coupon testings models should be the same as the one in the real-components analysis which is 10 × 10 mm. However, due to the limited dimensions of gauge length and specimen sizes, an element size of 10 × 10 mm is unsuitable for all coupon testing specimens.

In this thesis, *MAT_058 and *MAT_124 material cards follow different element sizes and they are explained in their respective sections. The configurations and dimensions of the specimens, support and punch in the FE models are consistent with the test conditions described in the Chapter 3.

4.4 Implementation of *MAT_058

The implementation of *MAT_058 was done by following steps:

1. Numerical models setup.
2. Classify variables into five groups.
3. Tension test simulation and optimisation.
4. Compression test simulation and optimisation.
5. In-plane shear test simulation and optimisation.
6. Four-point flexural test simulation and optimisation.

Optimal parameters that were obtained from the early steps were set to constant in the later steps.

This process of optimising one test at a time is possible since the parameters in **MAT_058* (apart from ERODS) are independent on the other loading conditions, see Section 4.4.2.

4.4.1 Numerical models setup

Meshing:

In the implementation of **MAT_058*, element size used for different models are listed in Table 4.2. In the tensile test model, the deformation was assumed to be uniform enough that a 10 mm gauge length would give similar result as a 8 mm gauge length in the coupon test. In the flexural test model, in order to keep the punches and supports as cylinders, the mesh size was chosen as 3×3 mm, considering that a uniform mesh size for punches, supports and specimen could avoid numerical errors.

Table 4.2: Element size used in **MAT_058* models.

Model	Tensile test	Compressive test	Shear test	Flexural test
Average element size (mm)	10×10	6×6	4×4	3×3

Boundary conditions:

The boundary conditions applied in the test models are presented as follows: Figure 4.1a, Figure 4.1b and Table 4.3 for tensile and compressive tests models; Figure 4.2a, Figure 4.2b and Table 4.4 for shear and flexural tests models. The following symbols are used in both tables:

- 0 = free
- 1 = constrained
- P.m. = Prescribed motion
- v = loading velocity (mm/s)

Except for specific explanation, all the constrained degrees of freedom were defined by **BOUNDARY_SPC* in LS-DYNA; and all the prescribed motions were defined by **BOUNDARY_PRESCRIBED_MOTION* on the boundaries nodes.

In the tensile and compressive tests models, since only the clamping-free part between two grips was of interest, the clamped parts of the specimen were not modelled in order to reduce computation time.

The velocity of prescribed motion in tensile test model was set to +1 mm/s so as to keep consistency with the actual testing strain rate.

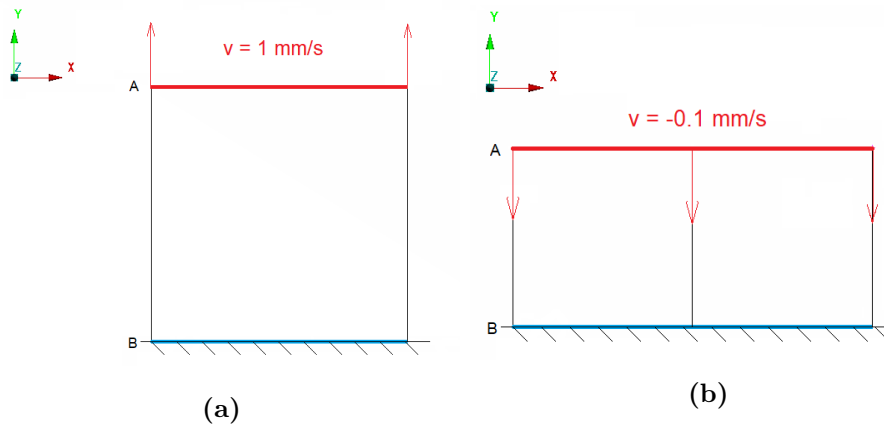


Figure 4.1: (a) Tensile test model (b) Compression test model. Boundary conditions are applied on edges A and B.

Table 4.3: Boundary conditions applied in the tensile test and compression model.

	Trans.X	Trans.Y	Trans.Z	Rot.X	Rot.Y	Rot.Z
Tensile test model						
Edge A	0	P.m ($v=+1$)	0	0	0	0
Edge B	1	1	1	1	1	1
Compression test model						
Edge A	0	P.m ($v=-0.1$)	0	0	0	0
Edge B	1	1	1	1	1	1

Tensile/ compressive stress was calculated by adding the forces of all the nodes on edge A and then dividing the cross-section area of the specimen. Tensile/ compressive strain was calculated by the displacement of one node on the loading edge dividing the original free length.

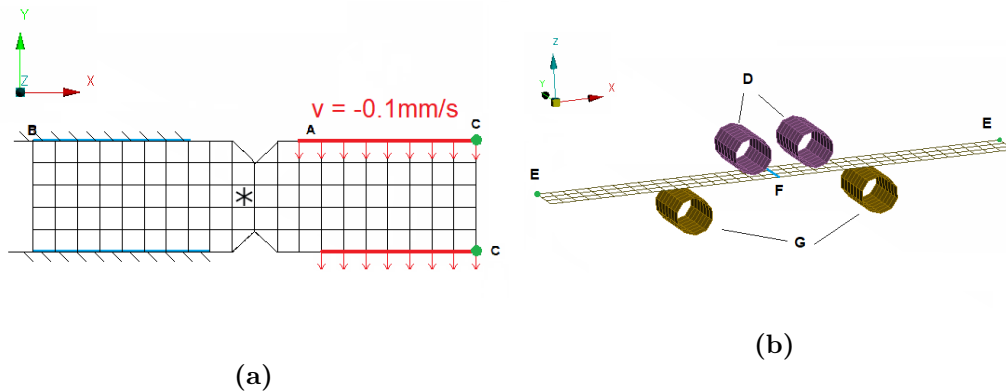


Figure 4.2: (a) Shear test model (b) Flexural test model. Boundary conditions are applied on: edges A, B and F; points C and E and rigid parts D and G.

The boundary condition in the shear test model was applied only for the nodes which were in contact to the fixture as shown in Figure 4.2a. Displacement con-

straints were applied along the fixture-to-specimen contact on the left part of the specimen to eliminate rigid body motion. Uniformly applied prescribed motion were applied along the fixture-to-specimen contact region on the right part of the specimen. Two nodes on the right side (marked as point C) were constrained in the translation x-direction to prevent the specimen from moving in horizontal direction.

According to Section 3.4, engineering shear stress and strain were calculated by Equations (4.1) and (4.2) respectively. The shear force was obtained by adding y-force of all the nodes that were in contact to the fixture. Cross-sectional area between the V-notches was used for dividing the force in Equation (4.1). Tensorial shear strain was obtained by reading ELOUT output (average xy strain) of the middle-left element between the V-notches (the element marked with '*' in Figure 4.2a). Engineering shear strain is twice tensorial shear strain, as shown in Equation (4.2).

Table 4.4: Boundary conditions applied in the shear and flexural tests models.

	Trans.X	Trans.Y	Trans.Z	Rot.X	Rot.Y	Rot.Z
Shear test model						
Edge A	0	P.m. (v=-0.1)	0	0	0	0
Edge B	1	1	1	1	1	1
Point C	1	0	0	0	0	0
Flexural test model						
Rigid part D	1	1	P.m (v=-0.4)	1	1	1
Point E	0	1	0	0	0	0
Edge F	1	0	0	0	0	0
Rigid part G	1	1	1	1	1	1

$$\sigma_{eng} = \frac{\text{Nodal forces}}{\text{Cross sectional area between V notches}} \quad (4.1)$$

$$\gamma = \varepsilon_{xy} * 2 \quad (4.2)$$

The loading span was modelled as one-thirds of support span in the flexural test model (Procedure A). Only the supporting and punching cylinders were modelled for simplification instead of the whole testing fixture. Both of them were modelled as rigid parts with **MAT_020 (*MAT_RIGID)*, boundary conditions of which were set in the variables CON1 and CON2 in **MAT_020*. For contact reason, they were seen as an arbitrary steel with $E = 210000$ MPa, $\rho = 7.85 \cdot 10^9$ ton/mm³ and $\nu = 0.3$. The loading of the punches were given in **BOUNDARY_PRESCRIBED_MOTION_RIGID*.

Two similar contact conditions were defined by using **CONTACT_AUTOMATIC_SURFACE_TO_SURFACE*: (1) between the supports and the specimen; (2) between the punches and the specimen. In both cases, the specimen was set to slave segment.

The static coefficient of friction was found to have a certain degree of influence on the results, which can be found in Chapter 5.

Flexural force was obtained by reading RCFORC output (Master contact) of the punches. Flexural deflection was obtained by reading the z-displacement of the middle node on edge F. Then, Flexural strain/ stress was calculated according to Table 3.1.

4.4.2 Classification of variables

From Table 2.1 in Chapter 2, it can be concluded that some variables simultaneously play important roles in the simulation where a certain type loading condition happens; for example, EA, E11T, XT, SLIMT1 and ERODS are the major variables that influence the uni-axial tension stress-strain relation, in which E11T and XT act as damage criteria and ERODS acts as failure criteria. Later, we also found out that MXEPS and EPSSH in **MAT_ADD_EROSION* (card 2) act better as failure criteria in curve matching. In this thesis, variables used in **MAT_058* and **MAT_ADD_EROSION* were divided into following five groups during implementation, as shown in Table 4.5.

Table 4.5: Classification of variables in **MAT_058* and **MAT_ADD_EROSION*.

	Variable Name	Source	Will be optimised?
Tension-related	EA (EB)	Experiment	No
	MXEPS	Experiment	
	E11T (E22T)	Experiment	Yes
	XT (YT)	Experiment	
	SLIMT1, SLIMT2	LS-DYNA Manual	
Compression-related	EA (EB)	Experiment	No
	MXEPS	Experiment	
	E11C (E22C)	Experiment	Yes
	XC (YC)	Experiment	
	SLIMC1, SLIMC2	LS-DYNA Manual	
In-plane shear-related	GAB	Experiment	No
	SC	Experiment	Yes
	GMS	Experiment	
	EPSSH	Experiment	
	SLIMS	LS-DYNA Manual	No
	FS	LS-DYNA Manual	
Flexural-related	GBC	Literature: [42]	Yes
Others	RO	Experiment	No
	PRBA	Experiment	

Variables EA, E11T, XT, E11C and XC describe material properties in the longi-

tudinal direction. The input of them were set to equal to the input for variables that describe the transverse direction (i.e. EB, E22T, YT, E22C, YC) due to the in-plane isotropic assumption.

4.4.3 **MAT_058* baseline model

Table 4.6 and Table 4.7 lists input for **MAT_058* and **MAT_ADD_EROSION*. Most of the values were taken from experimental data, except for SLIMxx which was taken as default values suggested by LS-DYNA Manual[22].

Table 4.6: Input for **MAT_058* baseline model.

MID	RO	EA	EB	(EC)	PRBA	TAU1	GAMMA1
	1.84E-9	-4002	-4002		0.225		
GAB	GBC	GCA	SLIMT1	SLIMC1	SLIMT2	SLIMC2	SLIMS
-7001	3200	3200	0.001	1	0.001	1	1
AOPT	TSIZE	ERODS	SOFT	FS	EPSF	EPSR	TSMD
0.0				1			
XP	YP	ZP	A1	A2	A3	PRCA	PRCB
V1	V2	V3	D1	D2	D3	BETA	
E11C	E11T	E22C	E22T	GMS			
0.0343	0.022	0.0343	0.022	0.0133			
XC	XT	YC	YT	SC			
172.72	110.5	172.72	110.5	73.1			

Table 4.7: Input for **MAT_ADD_EROSION* of **MAT_058* baseline model.

MNPRES	SIGP1	SIGVM	MXEPS	EPSSH	SIGTH	IMPULSE	FAILTM
			0.0254	0.0243			

The detailed description of the variables are listed as follows:

EA (EB):

Young's modulus, by definition, is the proportionality between stress and strain of a material under linear elastic deformation, which is described by Hooke's law as

$$E = \frac{\sigma}{\epsilon}, \quad (4.3)$$

where E is Young's modulus; σ is the uniaxial stress; ϵ is strain and it is unitless. The following sign convention is used: tensile stresses and strains are positive, compressive stress and strains are negative.

In the baseline model, a load curve (curve ID: 4002) was input for Young's modulus in both longitudinal and transverse directions. The curve is shown in Figure 4.3 and it consists of both tension (positive data points) and compression (negative data points) engineering curves, according to [43].

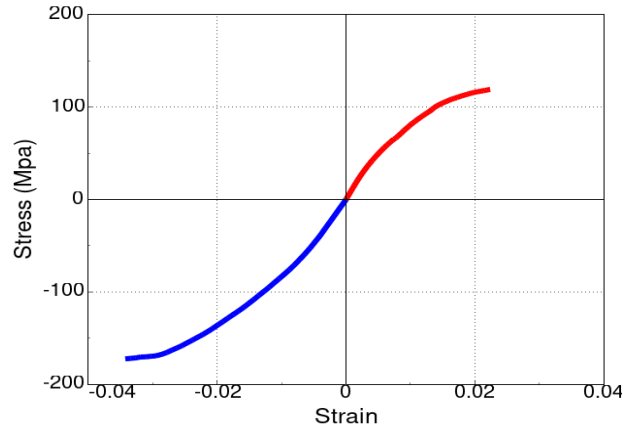


Figure 4.3: Load curve (curve ID: 4002) input for Young's modulus EA and EB.

In addition, from a mathematical point of view, since each strain value has only one stress value associated with it (and vice versa), all the points after maximum stress (absolute value) were removed in the input curve.

E11T (E22T), E11C (E22C) and GMS:

Strain (absolute value) at maximum stress for tensile, compression and shear, which were taken from respective test. They act as damage criteria.

XT (YT), XC (YC) and SC:

Maximum stress (absolute value) for tensile, compression and shear, which were taken from respective test.

SLIMT1 (SLIMT2), LIMC1 (SLIMC2) and SLIMS:

LS-DYNA Manual [22] recommends values for SLIMT1 (SLIMT2) and SLIMC1 (SLIMC2) as 0.001 and 1 respectively. Based on the description in Section 2.3.1.1 and the experimental shear curve, SLIMS=1 was chosen as a preliminary value.

MXEPS:

Maximum principal strain at failure, ϵ_{max} , which acts as failure criteria.

GAB:

An experimental engineering in-plane shear stress-strain curve (curve ID: 7001) was input for in-plane shear modulus, as shown in Figure 4.4, in which all the data points are positive, according to [43].

EPSSH:

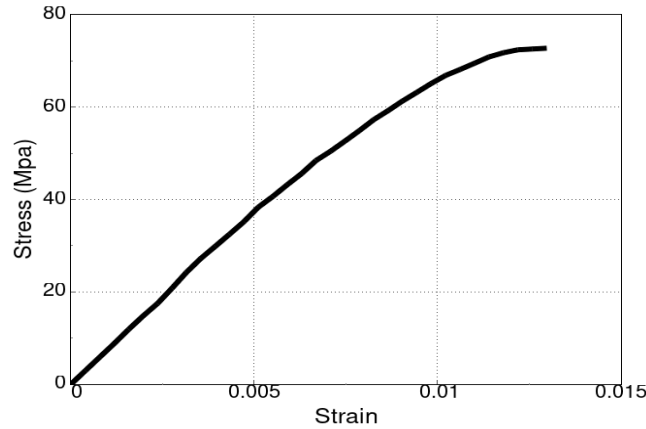


Figure 4.4: Load curve (curve ID: 7001) input for in-plane shear modulus GAB.

Shear strain at failure, γ_{max} , which acts as failure criteria.

FS:

FS acts as a flag for choosing failure surface type. In this thesis, FS was chosen as 1.

GBC (GAC):

Since out-of plane shear modulus was not measured in the coupon testings, a preliminary value of 3200 MPa (suggested by [42]) was used as input for GBC and GAC. GBC (GAC) will be optimised in the optimisation step.

Static coefficient of friction in **CONTACT*:

[44] found out that the static coefficient of friction between glass fibre reinforced plastic and stainless steel is between 0.05 and 0.13. A preliminary value of 0.1 was input in the baseline model.

4.4.4 optimisation of **MAT_058* in Ls-Opt

The first step in the optimisation process was the selection of meta-model and optimisation strategy in Ls-Opt, for the optimisation of **MAT_058* material card the Metamodel-based optimisation with Successive Response Surface Method (SRS) strategy has been selected (By default Single Iteration strategy would be selected, the reason for selecting SRS strategy is described in Section 2.4.1). Figure 4.5 shows a flowchart about optimisation process in Ls-Opt.

Next step is to set the upper bound and lower bound under "Parameter setup" for the parameters listed in Table 4.5 (The values for lower and upper bound is listed in Chapter 5). Based on the number of parameters, number of simulation points is assigned by Ls-Opt. The method of Point selection needs to be defined by the user, for the optimisation of **MAT_058*, the default option "D-optimal" was used.

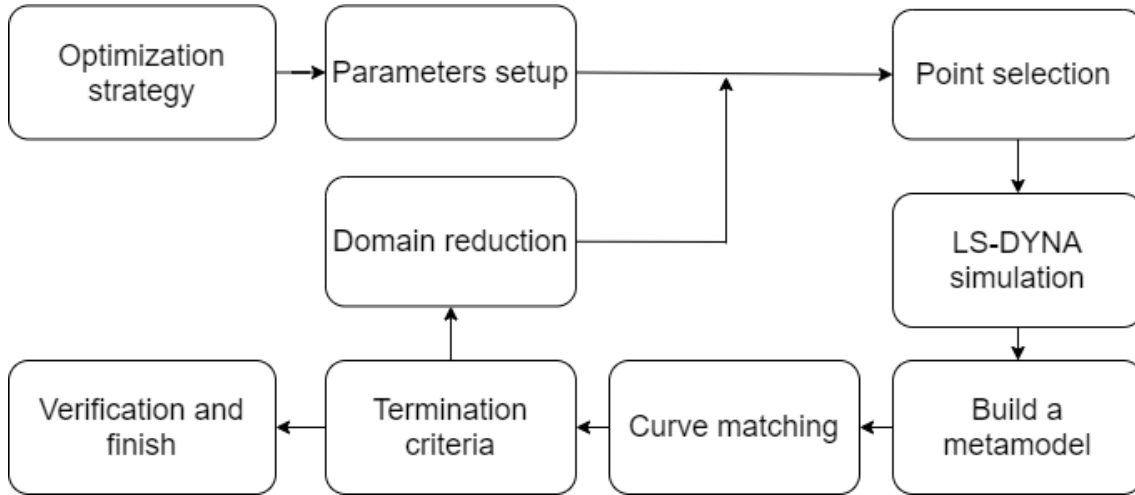


Figure 4.5: Schematic flowchart of Ls-Opt.

After the Point selection step, Ls-Opt assigns a set of values within the bounds for the listed parameters and performs the LS-DYNA simulations. Based on the output from the simulation, Ls-Opt builds a meta model and uses a curve mapping algorithm to evaluate area between the experimental curve and the simulation curve.

If the simulation curve result meets the user defined criteria, then Ls-Opt will verify the result and stops the optimisation process. If the user defined criteria is not met, then the *SRS*M strategy of domain reduction formulation is implemented by Ls-Opt for the set of values listed in "Parameter setup". It assigns a new set of values for the parameters and follows the same procedure until the user defined criteria is met.

Figure 4.6 is a Graphical User Interface (GUI) example of Ls-Opt for optimising shear-related variables in **MAT_058*.

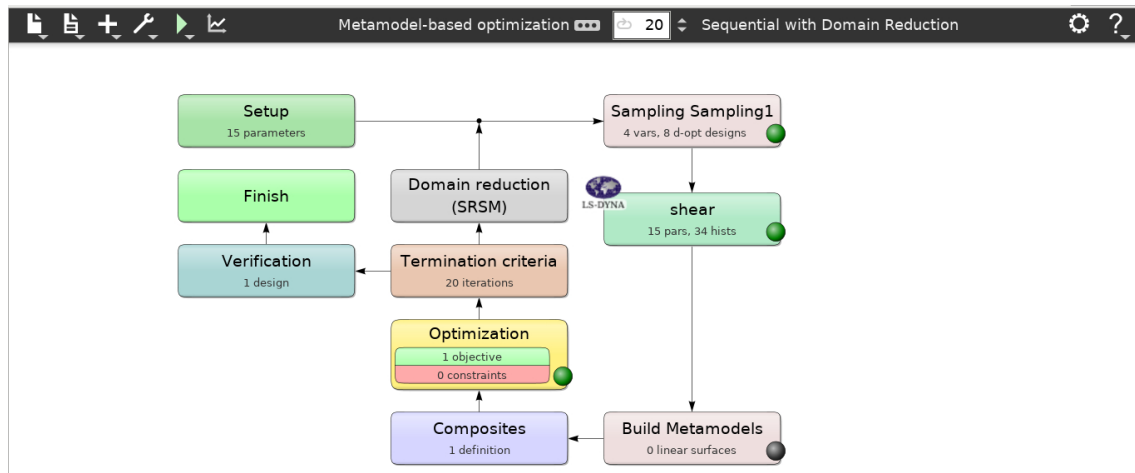


Figure 4.6: An example of Ls-Opt for optimising shear-related variables in **MAT_058*.

4.5 Implementation of **MAT_124*

Meshing strategy:

The final result of a Finite Element Analysis is influenced by a lot of parameters, mesh density is one such parameter which is complex to perceive and affects the accuracy of the model greatly [45]. Element size of the test specimen used for all four test cases simulated using **MAT_124* material card is listed in Table 4.8. To perform mesh regularisation utilised in *GISSMO* damage model, additional tensile test specimens with 0.5, 1, 2, 3, 5, 10 mm element size was modelled. 3 mm element size provided good result when compared to global element size of 10 mm and also mesh regularisation was planned initially, so an average of 3 mm element size has been used for tests specimens while implementing **MAT_124*.

Table 4.8: Element size used in **MAT_124* models.

Model	Tensile test	Compression test	Shear test	Flexural test
Average element size (mm)	3 × 3	3 × 3	4 × 4	3 × 3

Boundary condition:

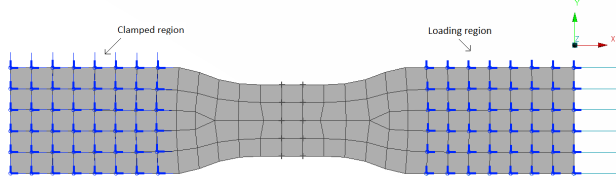
The boundary conditions applied for four test cases (in **MAT_124*) is presented below and the following variables are used to differentiate between the sides which are constrained and free to move:

- 0 = Free.
- 1 = Constrained.
- vel. = Loading velocity.

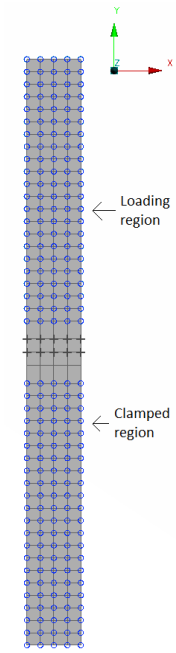
The tensile test specimen used for the simulation is as shown in Figure 4.7(a) and the boundary condition is as stated in Table 4.9. Similarly, the compression test specimen and its boundary condition is as shown in Figure 4.7(b) and Table 4.10 respectively. As explained earlier **BOUNDARY_SPC* was used for constraining the nodes and **BOUNDARY_PRESCRIBED_MOTION* was used for assigning velocity to the nodes.

Table 4.9: Boundary condition applied for tensile test case.

Tensile test case	Trans. X	Trans. Y	Trans. Z	Rot. X	Rot. Y	Rot. Z
Clamped region (*B_S)	1	1	1	1	1	1
Loading region (*B_S)	-	-	1	1	1	1
Loading region (*B_P_M)	vel.= 0.08 mm/s	-	-	-	-	-



(a) Tensile test specimen.



(b) Compression test specimen.

Figure 4.7: Models of (a) tensile test specimen and (b) compression test specimen.

Table 4.10: Boundary condition applied for compression test case.

Compression test case	Trans. X	Trans. Y	Trans. Z	Rot. X	Rot. Y	Rot. Z
Clamped region (*B_S)	1	1	1	1	1	1
Loading region (*B_S)	1	-	1	1	1	1
Loading region (*B_P_M)	-	vel.= -0.08 mm/s	-	-	-	-

As explained in Section 3.2 the engineering tensile stress was calculated according to the Equation (4.4), where the cross sectional force in the numerator was calculated by reading the SECFORC data from the post-processor. The engineering tensile strain was calculated according to the Equation (4.5). Where the displacement of two nodes is read from NODOUT data from the post-processor and divided it by the original distance between those two nodes.

$$\sigma_{eng} = \frac{\text{Cross sectional force}}{\text{Cross sectional area}} \quad (4.4)$$

$$\varepsilon_{eng} = \frac{\text{gauge}_x - \text{gauge}_y}{\text{Gauge length}} \quad (4.5)$$

The engineering stress and strain for compression test was calculated similarly to tensile test case using the Equation (4.6) and (4.7) respectively.

$$\sigma_{eng} = \frac{\text{Cross sectional force}}{\text{Cross sectional area}} \quad (4.6)$$

$$\varepsilon_{eng} = \frac{\text{gauge}_x - \text{gauge}_y}{\text{Gauge length}} \quad (4.7)$$

The shear test specimen used for the simulation is as shown in Figure 4.8. Boundary condition in shear test case is applied only for the nodes which will be in contact to the fixture as shown in Figure 3.4. Table 4.11 shown below is the boundary condition applied for these nodes.

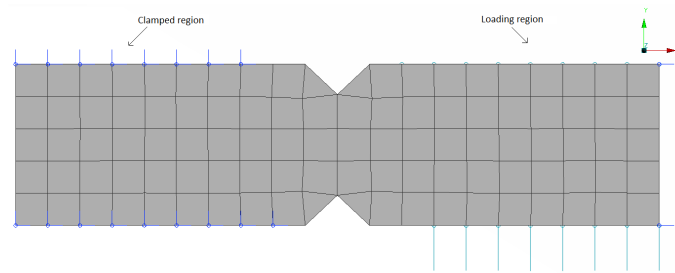


Figure 4.8: Shear test specimen.

Table 4.11: Boundary condition applied for shear test case.

Shear test case	Trans. X	Trans. Y	Trans. Z	Rot. X	Rot. Y	Rot. Z
Clamped region (*B_S)	1	1	1	-	-	-
Loading region (*B_S)	1	-	1	-	-	-
Loading region (*B_P_M)	-	vel.= -0.06 mm/s	-	-	-	-

The shear stress and strain were calculated in the same way as **MAT_058* described above in Section 4.4.1.

The contact condition, material property of the support and punch remains same as explained in the previous section for **MAT_058*. But the load span, loading speed and co-ordinate system was different for **MAT_124*. The test report did not provide enough details about the load span implemented for the physical coupon test and **MAT_124* showed good behaviour under one half load span. Hence one half load span test setup was used for the simulation and optimisation of **MAT_124* material card. The flexural test specimen and it's boundary condition is as shown in Figure 4.9 and Table 4.12 respectively.

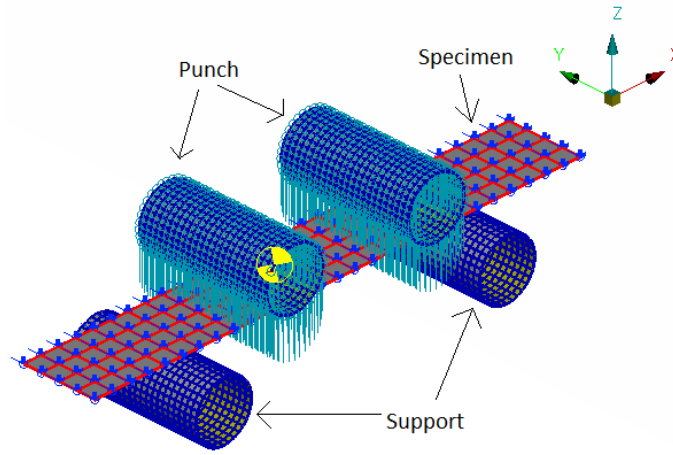


Figure 4.9: Flexural test specimen.

Table 4.12: Boundary condition applied for flexural test case.

Flexural test case	Trans. X	Trans. Y	Trans. Z	Rot. X	Rot. Y	Rot. Z
Specimen (*B_S)	-	1	-	1	-	1
Loading region (*B_P_M)	-	-	vel.= -0.6 mm/s	-	-	-

As explained in Table 3.1, for 1/2 load span length the engineering stress and strain for flexural test was calculated according to the Equation (4.8) and (4.9) respectively. Where the force exerted by the punch was taken into consideration while calculating the flexural stress by reading the RCFORC data from the post-processor. While NODOUT data from the post-processor was used to calculate the displacement of the specimen's middle node for the calculation of flexural strain.

$$\sigma_{eng} = \frac{3 * Resultant\ master\ force * Support\ span}{4 * Width\ of\ the\ specimen * Thickness\ of\ the\ specimen^2} \quad (4.8)$$

$$\varepsilon_{eng} = \frac{4.36 * Nodal\ displacement * Thickness\ of\ the\ specimen}{Support\ span^2} \quad (4.9)$$

Load rate:

The quasi-static loading condition utilised by the testing center to perform the physical coupon test of all four test cases is presented in Chapter 3. While performing the virtual simulations using explicit method i.e., Central Difference Scheme, physical quasi-static test speed leads to a very small time steps. As a result it is computationally expensive to perform the simulation quasi-statically.

From trial and error, the following test speed listed in Table 4.13 was valid enough to run the simulation to avoid dynamic affect during the virtual simulation using *MAT_124 material card.

Table 4.13: Load rate for all four test case in **MAT_124* material card.

Test case	Velocity (mm/s)
Tensile test	0.08
Compression test	0.08
Shear test	0.06
Flexural test	0.6

4.5.1 **MAT_124* baseline model

After meshing, prescribing boundary and loading conditions to the model, next step was to feed the material card with test data and necessary parameters. In the following Table 2.3 the variables RO , E , PR , EC , $LCIDT$, $LCIDC$, $RPCT$, PC and PT are obtained from the physical coupon test results.

Young's modulus in tension E and compression EC was set as parameters in Ls-Opt to fit the simulation test result to the experimental test result. For the baseline model optimisation, Young's modulus in tension is selected from 0.1 s^{-1} strain rate case. It is worth to mention that compression coupon test was not performed for different strain rate values.

Depending on PC and PT value, the shear and bending test will follow $LCIDT$ or $LCIDC$ hardening curve. Generally PC and PT is calculated from the yield stress value obtained from physical test i.e., $PT = \sigma_{yt}/3$ and $PC = \sigma_{yc}/3$. $RPCT$ depends on the ratio of PT to PC . Table 4.14 represents the parameters in **MAT_124* that are optimised in Ls-Opt. As each physical test case was performed using five test specimens, the lower and upper bounds for the parameters listed in Table 4.14 was assigned based on the set of experimental values observed in each specimens.

Table 4.14: Parameters to be optimised in **MAT_124*.

	Variable name	Source of the value	Will be optimised?
Tension-related	E	Experiment	Yes
	PT	Experiment	
	LCIDT	LS-DYNA manual	No
	LCSRT	LS-DYNA manual	
Compression-related	EC	Experiment	Yes
	PC	Experiment	
	LCIDC	LS-DYNA manual	No
Other	PR	Experiment	Yes
	RPCT	LS-DYNA manual	

Hardening curve:

As explained in Section 2.3.2, plasticity in the material is captured using **MAT_124* material model. This material model is built on the von Mises flow rule, where the hardening/yield curve has to be determined from the physical test result. The

engineering stress-strain curve from the physical test result can be converted to true stress-strain curve using the Equation (4.10) and (4.11).

$$\sigma_{true} = \sigma_{eng}(1 + \varepsilon_{eng}) \quad (4.10)$$

$$\varepsilon_{true} = \ln(1 + \varepsilon_{eng}) \quad (4.11)$$

To plot the "Effective Trues Stress vs Effective True Plastic Strain" in tension and compression case used to input *LCIDT* and *LCIDC* variables, effective plastic true strain needs to be calculated using the Equation (4.12) (it was calculated after the material reaches yield stress). This equation can provide "Effective Trues Stress vs Effective True Plastic Strain" data until the material reaches it's ultimate strength. To determine the amount of plastic deformation occurred in the material it was necessary to capture data beyond the ultimate strength point. This can be achieved by extrapolating the curve beyond ultimate strength using various methods such as Hockett-Sherby, Stoughton-Yoon, Estrin-Mecking, Shift, Bergstrom etc., extrapolation techniques. In this thesis work, Bergstrom extrapolation technique was implemented to plot "Effective Trues Stress vs Effective True Plastic Strain".

$$\varepsilon_{true,plast} = \varepsilon_{true} - \frac{\sigma_{true}}{E} \quad (4.12)$$

The "Effective true stress vs Effective true plastic strain" curves in tension and compression case is calculated as explained above, Figure 4.10 and Figure 4.11 shown below are the hardening curves used in this thesis work.

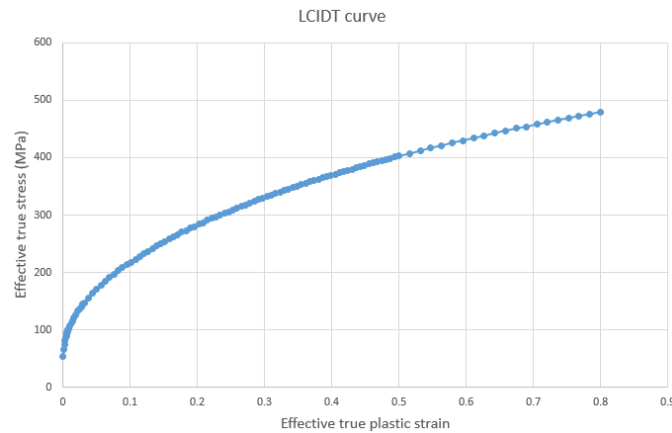


Figure 4.10: Effective true stress vs Effective true plastic strain in tension (LCIDT).

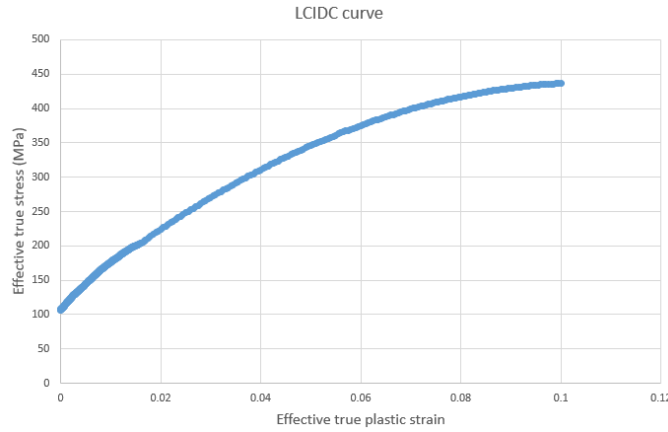


Figure 4.11: Effective true stress vs Effective true plastic strain in compression (LCIDC).

Strain Rate:

To implement strain rate dependency in the constitutive model, strain rate parameters P and C for Cowper-Symonds model or pressure cut-off parameters in tension ($PCUTT$) and compression ($PCUTC$) or load curve $LCSRT$ and $LCSRC$ defining strain rate factor on "Yield stress vs Strain rate" in tension and compression respectively must be used. Since physical coupon test is conducted for different strain rates in tensile test case, in this thesis work only $LCSRT$ curve was provided for the virtual simulations. Figure 4.12 is the "Yield stress vs Strain rate" curve used in this thesis work. But due to lack of time, this curve was not optimised. Hence strain rate effect was not investigated using **MAT_124*.

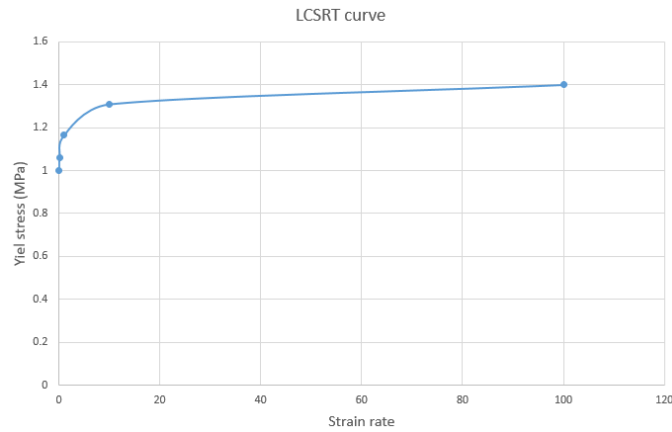


Figure 4.12: Yield stress vs Strain rate (LCSRT).

Failure criteria:

This material card provides user an option to define failure in the material either by defining plastic strain to failure (*FAIL*) or minimum time step size for automatic element deletion (*TDEL*). Since effective plastic strain to failure value varies from one test case to another, *FAIL* variable is generally not recommended.

Optional parameters:

The optional parameters K used for viscoelastic materials, G_i used as shear relaxation modulus for the i^{th} term and $BETA_i$ used as shear decay constant for the i^{th} term are not used for any simulation in this thesis work.

4.5.2 Optimisation of **MAT_124*

All four test cases performed in the physical coupon test was simulated in LS-DYNA individually to analyse how the specimen responds to the prescribed boundary and loading condition. Next step was to optimise the parameters listed in Table 4.14 using Ls-Opt. The method followed for optimising **MAT_124* remains same as described in Section 4.4.4. But for **MAT_124*, based on trial and error, "Latin Hypercube" point selection was used as it provided better result compared to the "D-Optimal" point selection which was a default method. Rest of the options used in Ls-Opt remains same for both **MAT_058* and **MAT_124*.

By optimising the parameters listed in Table 4.14 for all four test cases in a single Ls-Opt file as shown in Figure 4.13, the material response for different stress state can be optimised as these parameters impact each test case.

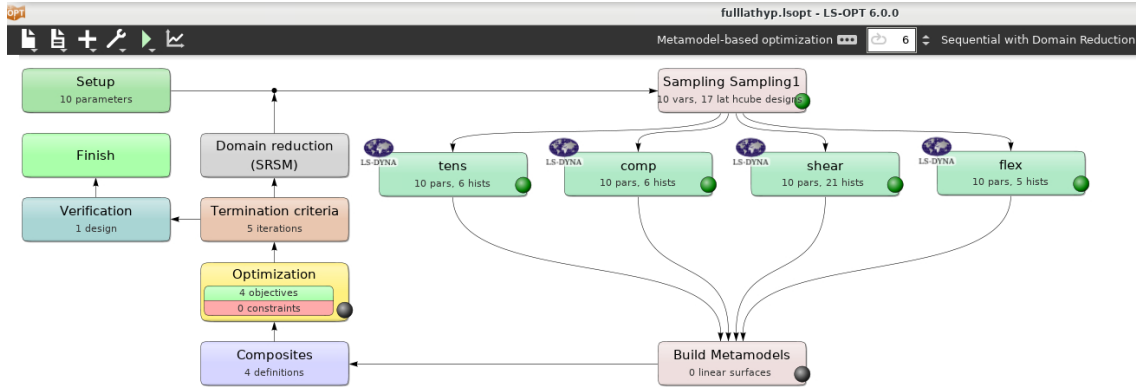


Figure 4.13: optimisation process using SRSM strategy.

4.5.3 Implementation of **MAT_ADD_EROSION*

Parameters for the baseline **MAT_124* material card was optimised as described in Section 4.5.2 and this optimised material card will capture the elasto-plastic response of the material, while **MAT_ADD_EROSION* will assist in gathering the accumulated damage data in the material after it reaches instability.

Card 1 and 2 consists of numerous failure criteria that can be defined as per user requirement, but for the current study they are not utilised. *IDAM* is a variable used to specify the damage model used in the analysis. When $IDAM = 0$, damage model is not used. When $IDAM = 1$, *GISSMO* damage model is activated and if $IDAM \leq 1$, *DIEM* damage model is activated. Since this study focuses only on *GISSMO* damage model $IDAM = 1$. The parameters in **MAT_ADD_EROSION*

that are optimised is shown in Table 4.15.

Table 4.15: Parameters to be optimised in **MAT_ADD_EROSION*.

	Variable name	Source of the value	Will be optimised?
GISSMO card related	LCSDG	Experiment	Yes
	ECRIT	Simulation	
	DMGEXP	Literature	
	FADEXP	Literature	
Other	NUMFIP	Literature	No
	LCREGD	Simulation	

Number of failed integration points:

Card 1 contains a variable *NUMFIP* which was used for element deletion when shell elements are used for modeling. $|NUMFIP|$ operates as the percentage of integration points through the thickness which must exceed the failure criteria before deleting an element from the simulation [22]. For the current study when 80% of the integration points has failed, stress-strain curve from virtual simulation fits well with the physical coupon test results and this is based on trial and error technique. So, $NUMFIP = -80$ was opted for all the simulations.

Equivalent plastic strain to failure vs. triaxiality (LCSDG):

Triaxiality dependent failure strain is a dominant factor in *GISSMO* damage model, so it was necessary to conduct physical coupon tests for a wide range of specimen shapes to capture broad spectrum of failure strain and triaxiality values. The experimental test described in Chapter 3 was conducted prior to this thesis work, so these tests were not conducted specifically to model *GISSMO* damage card.

The triaxiality value for the four virtual coupon tests in this study is listed in Table 4.16. These values are taken from the simulation result when the triaxiality is constant up to a critical load value and they are validated based on the literature [46]–[48]. It is arguable that triaxiality will not be exactly as described in the Table 4.16, but it was a simplification made in this study for curve fitting the experimental and theoretical results.

Table 4.16: Triaxiality value for four test case considered in this thesis work.

Load case	Triaxiality
Uniaxial tension	1/3
Uniaxial compression	-1/3
Shear	0
Flexural	1/2

To get the initial values for the plastic strain to failure, the following procedure was used. During the simulation (for every test case) using baseline **MAT_124* material card, the first element which captures highest stress was considered as a "Critical

element". For all four test cases the plastic strain in the "Critical element" was measured when load drops from it's maximum point and was noted as the "Equivalent plastic strain" for that particular test case. Then the triaxiality values from the Table 4.16 and "Equivalent plastic strain" from respective test case was used to plot the "Equivalent plastic strain to failure vs. triaxiality" (*LCSDG*) curve. For curve fitting purpose the equivalent plastic strain to failure values were identified as parameters that needs to be optimised in Ls-Opt, the *LCSDG* curve before optimisation is shown in Figure 4.14.

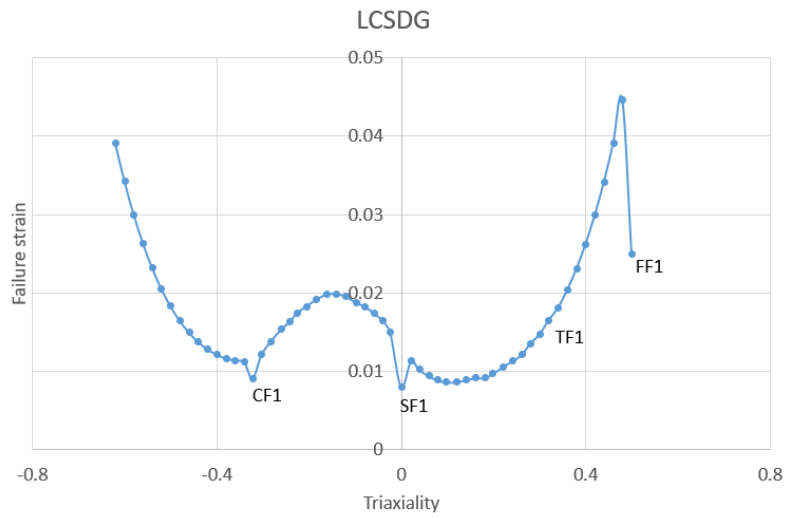


Figure 4.14: Failure strain vs triaxiality curve before optimisation (*LCSDG*).

Critical equivalent plastic strain vs triaxiality (*ECRIT*):

The instability measurement in the material (ΔF) described in Equation (2.20) depends mainly on the *ECRIT* curve. However, theoretical triaxiality value (From Table 4.16) was not taken into consideration while plotting *ECRIT* curve. Instead, the triaxiality path of the "Critical element" was examined. When there was a slight spike or variation in the stress triaxiality path, the triaxiality and strain value at that particular time step was noted down. The strain value at that time step was considered as "Critical equivalent plastic strain".

This procedure remains same for all four test cases and this critical strain and triaxiality values was used to plot *ECRIT* curve. As instability in the material is triggered after the material reaches critical strain value, it was necessary to optimise this value. Hence critical equivalent plastic strain was set as a parameter in the Ls-Opt, the *ECRIT* curve before optimisation is shown in Figure 4.15.

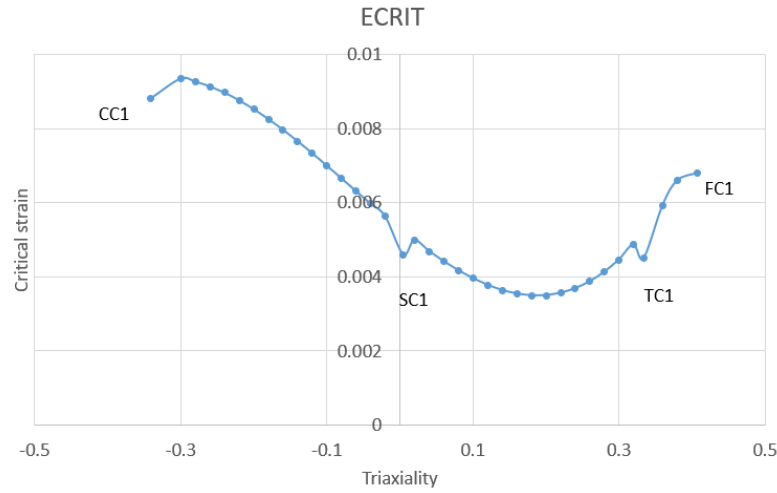


Figure 4.15: Critical strain vs triaxiality curve before optimisation (ECRIT).

Damage and Fading exponents:

As explained in Section 2.3.3.1, both damage exponent ($DMGEXP$) and Fading exponent ($FADEXP$) are nonlinear values. From Equation (2.20) and (2.22) it is clear that $DMGEXP$ and $FADEXP$ are interdependent. In the Figure 4.16 the red curve has $DMGEXP = 2$ and $FADEXP = 2$, for these values the material has accumulated damage until 0.022 strain and then fails. Similarly for the purple curve $DMGEXP = 4$, $FADEXP = 6$ and for this value the material has accumulated damage until 0.025 strain and failed. A wide range of values for $DMGEXP$ and $FADEXP$ has been simulated and the results are shown in Figure 4.16. From the Figure 4.16 it can be inferred that there is no definite value for $DMGEXP$ and $FADEXP$, hence they are determined by reverse engineering process using optimisation technique.

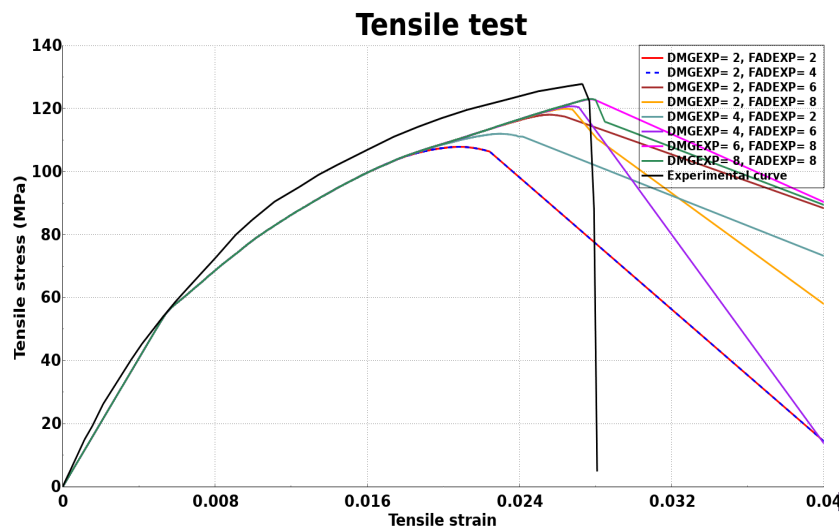


Figure 4.16: Stress vs strain values for different set of $DMGEXP$ and $FADEXP$ values.

Mesh Regularisation:

In general, the above described parameters were optimised for a specific element size. In this study, the baseline **MAT_124* and **MAT_ADD_EROSION* material card was optimised for 3 mm (in tensile, compression and flexural test) and 4 mm (in shear test) element size. For each test case, based on the material property and type of element formulation, failure/plastic strain value varied for different element size. To make sure that the optimised **MAT_124* and **MAT_ADD_EROSION* material card gives the same result when the element size is varied, it was necessary to perform mesh regularisation. This was done by modelling the tensile test specimen with 0.5, 1, 2, 3, 5, 10 mm element size (element size range should be within the global element size used for the application). Virtual tensile test for these six element sizes was performed and the "Critical element" was marked in each model to evaluate the failure strain value. The equivalent plastic strain for each element size was later normalised to plot the "Scale factor vs Element size" (*LCREGD*) curve. *LCREGD* curve operates as a scaling factor for the *LCSDG* curve. Figure 4.17 shown below is the "Scale factor vs Element size" curve before optimisation. Due to time constraint, this curve was not optimised.

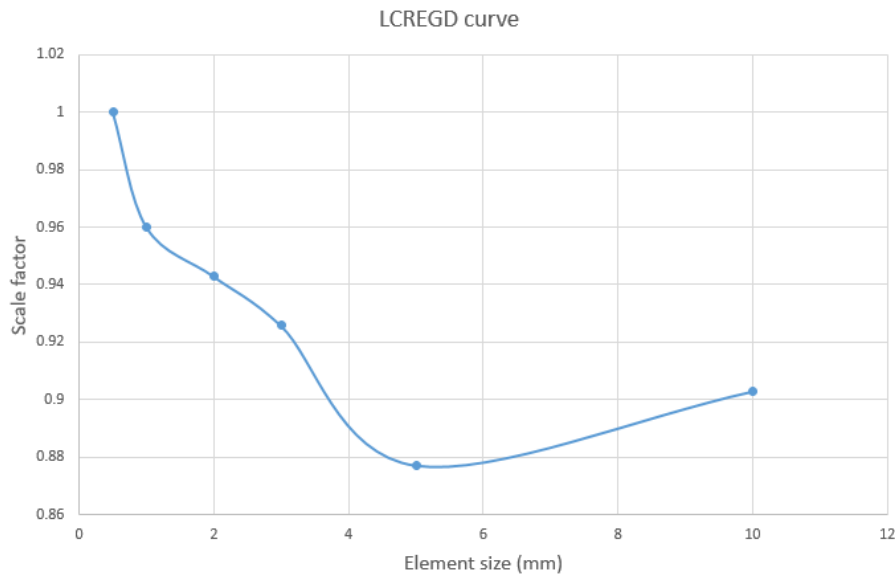


Figure 4.17: Scale factor vs Element size curve.

4.5.4 Optimisation of **MAT_ADD_EROSION*

The method followed for the optimisation of **MAT_ADD_EROSION* is same as explained in Section 4.5.2. The results from the final optimisation is presented in Chapter 5.

5

Optimisation result and discussion

This chapter presents the parameter optimisation setups and the coupon testings' simulation results of **MAT_058* and **MAT_124*.

5.1 Calibration results of **MAT_058*

5.1.1 Tension test simulation

The optimising ranges and optimal values for variables of interest is shown in Table 5.1. Lower and upper bound were initially defined according to the average value and standard deviation from the experimental results, then a wider range for E11T was set to find a better match. However, bounds for SLIMT1 and SLIMT2 were given by LS-DYNA Manual [22].

Table 5.1: Setup and results for tension-related variables in **MAT_058*.

	Lower bound	Baseline model	Upper bound	Optimal value
E11T (E22T)	0.008	0.0229	0.0260	0.0115665
XT (YT)	114	119.7	125	117.876
SLIMT1	0.001	0.001	1	0.18378
SLIMT2	0.001	0.001	1	0.276262
MXEPS	-	0.0254	-	0.0254

The tension test simulation results of **MAT_058* baseline model and optimised result are shown in Figure 5.1a. The optimised curve (blue curve) is quite close to the experimental curve. It is able to capture the non-linear stress-strain relation and predict the maximum tensile stress. However, the material is slightly stiffer than it is in the reality after damage initiation.

Figure 5.1b shows the simulation result where a constant value 11206 (which was mentioned in Table 3.2) was input for Young's modulus EA and EB, while the input of all the rest variables were the same as in baseline model. The purple curve shows a good match with the experimental curve with slightly over-stiff behaviour before and after the damage initiation, compared with the blue curve.

5. Optimisation result and discussion

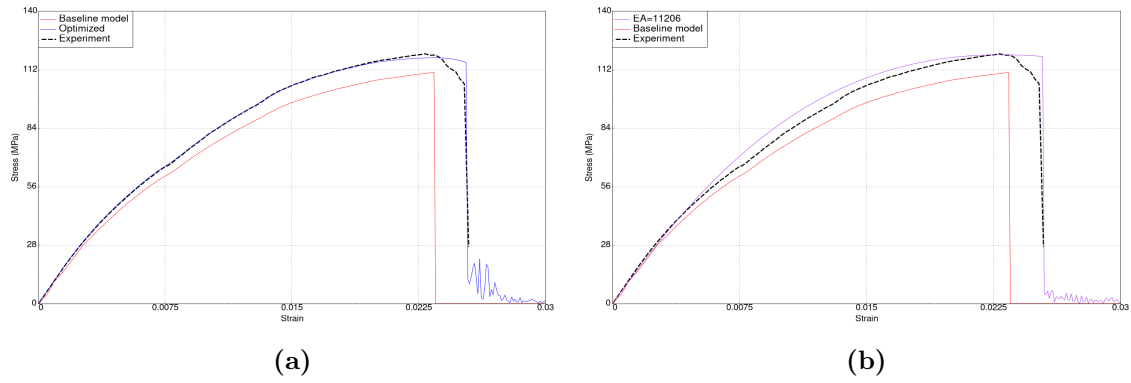


Figure 5.1: (a) Tensile test simulation results using **MAT_058* (b) a constant value as input for Young's modulus EA.

Overall, the blue curve in Figure 5.1a is recommended.

5.1.2 Compression test simulation

Compression-related variables optimisation setup and results is listed in Table 5.2. The bounds were initially defined from the experimental average values and standard deviation, then a wider range was set in order to find a better match.

Table 5.2: Setup and results for compression-related variables in **MAT_058*.

	Lower bound	Baseline model	Upper bound	Optimal value
E11C (E22C)	0.022	0.0343	0.04	0.035
XC (YC)	160	172.72	194	162
SLIMC1	0.001	1	1	0.415743
SLIMC2	0.001	1	1	0.446531

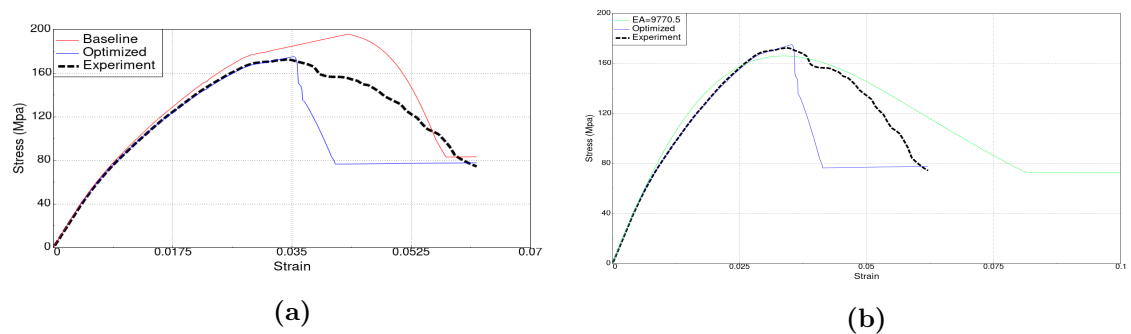


Figure 5.2: (a) Compression test simulation results using **MAT_058* (b) a constant value as input for Young's modulus EA.

The compression test simulation results of **MAT_058* baseline model and optimised result are shown in Figure 5.2a. In the time-frame of this thesis, the blue optimal

material model is found out to be the best match. It captures an excellent stress-strain behaviour until damage initiation. However, the damage degradation couldn't be well predicted. In the reality, the material could withstand larger deformation, and therefore the material would absorb more energy before it completely fails.

Similar to the previous section, a constant value 9770.5 (which was mentioned in Table 3.2) was input for Young's modulus EA and EB, while the input of all the rest variables were the optimal values, which is shown in Figure 5.2b. The green curve shows a better yet stiffer after-damage prediction than the blue curve. However, the green curve is not able to capture the maximum compressive stress and it absorbs too much energy before failure, which is not conservative.

Overall, the blue curve in Figure 5.2a is considered to be the best match.

5.1.3 In-plane shear test simulation

The optimising ranges and optimal values for shear-related variables are listed in Table 5.3. The bounds were found from the experimental average values and standard deviation.

Table 5.3: Setup and results for in-plane shear-related variables in **MAT_058*.

	Lower bound	Baseline model	Upper bound	Optimal value
SC	65	73.1	75	71.9263
GMS	0.0093	0.0133	0.014	0.0125672
EPSSH	0.015	0.0243	0.03	0.02928
SLIMS	0.001	1	1	0.802488

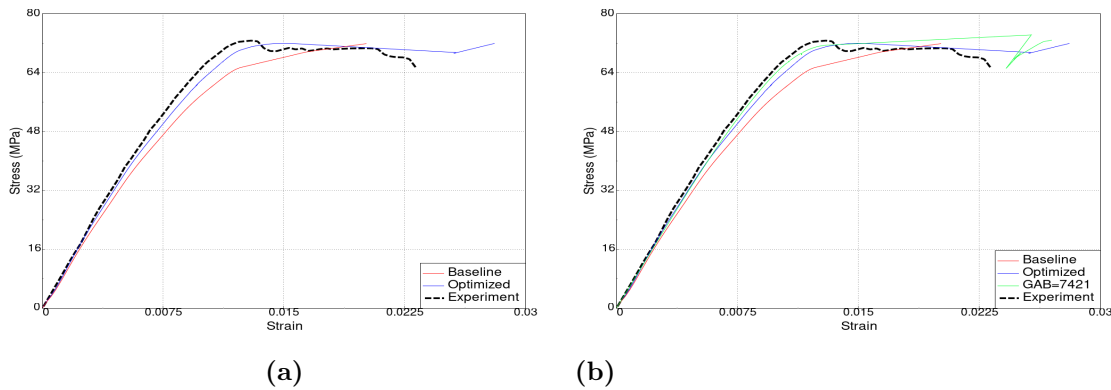


Figure 5.3: (a) Shear test simulation results using **MAT_058* (b) a constant value as input for shear modulus GAB.

The shear test simulation results of **MAT_058* baseline model and optimised results are shown in Figure 5.3a. The optimised (blue) curve predicts a conservative shear stress before the damage initiation. And after that, it predicts higher shear stress

than the experiment.

The green curve in Figure 5.3b was plotted by using a constant value 7421 (which was mentioned in Table 3.2) as input for shear modulus GAB, and optimal values as input for all the rest variables. The shear stress in the green curve keeps increasing and reaches the maximum shear stress after damage initiation, which shows an unconservative result.

Overall, the blue curve in Figure 5.3a is recommended as the best match.

5.1.4 Flexural test simulation

The optimising ranges and optimal values for flexural-related variables is listed in Table 5.4. The bound for the coefficient of friction (FC) was initially suggested by [44], which was between 0.05 and 0.13, then a wider range was used to find a better match.

It is found that the specimen failed due to tension in the flexural testing simulation. As a result, tension-related variables have influence on the flexural testing result. In addition, out-of-plane shear modulus GBC and GAC influence the result as well because the specimen was bent in that direction. The value of GBC equals to that of GAC due to the in-plane isotropic assumption. However, a too stiff GBC value (i.e. over 10000) would terminate the flexural test simulation before any flexural stress captured. Thus, the upper bound for GBC was chosen as 10000.

Table 5.4: Setup and results for flexural-related variables in **MAT_058*.

	Lower bound	Baseline model	Upper bound	Optimal value
GBC (GAC)	1000	3200	10000	5069
FC	0.01	0.1	0.2	0.03624

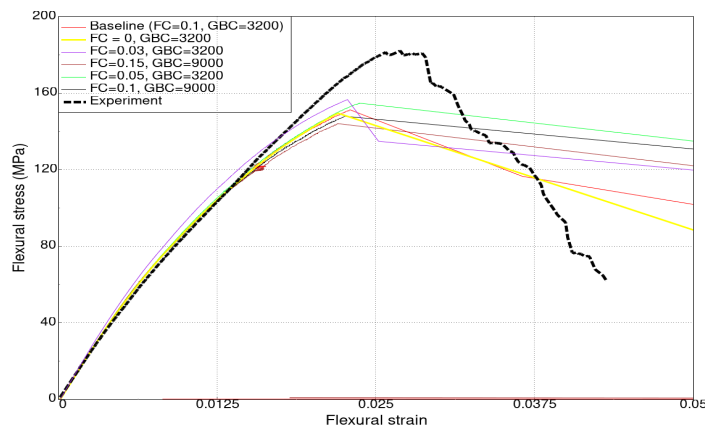


Figure 5.4: Flexural test simulation results using **MAT_058*.

The flexural test simulation results of **MAT_058* baseline model and parametric study on FC and GBC are shown in Figure 5.4. In general, a higher GBC value and a higher FC value would decrease the maximum flexural stress. However, adjusting the values of them was not able to give a perfect match with the experiment curve. This might because of the limitation of **MAT_058* material card, or might be due to improper FEM model.

Overall, the green curve in Figure 5.4 is considered as the best match.

5.2 Calibration results of **MAT_124*

5.2.1 Tension test simulation

Optimised result for tensile test with **MAT_124* and **MAT_124 + *MAT_ADD_EROSION* material card is shown in Figure 5.5. The optimised parameters related to tension test along with lower and higher bounds used in Ls-Opt is shown in Table 5.5.

Table 5.5: Setup and results for tension-related variables in **MAT_124* and **MAT_ADD_EROSION*.

	Lower bound	Baseline model	Upper bound	Optimal value
E	10000	10000	12000	10000.1
PT	16	16	20	17.8224
TC1	0.0045	0.0045	0.0164	0.00693061
TF1	0.0165	0.0165	0.025	0.0224635

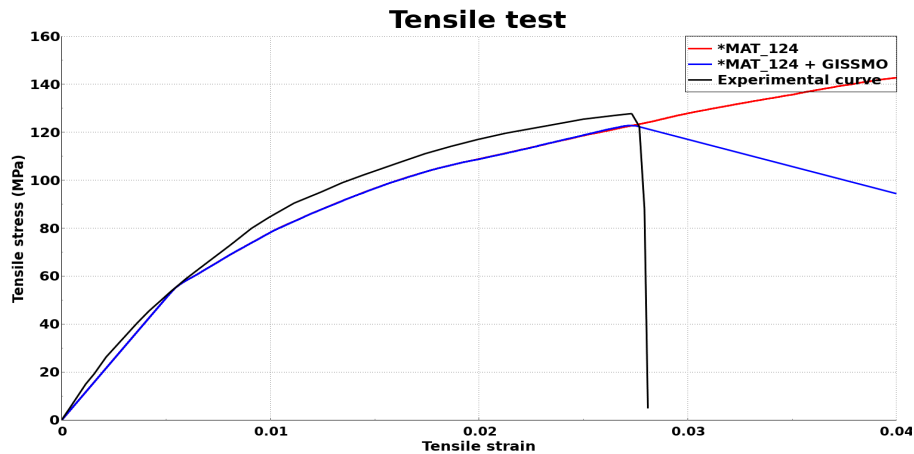


Figure 5.5: Tensile test simulation results using **MAT_124* and GISSMO.

Table 5.6: Error calculation in tensile test simulation.

Tensile test	Experimental value	optimisation value	Error
Failure stress (MPa)	128	122.5	4.4%
Failure strain	0.02736	0.02736	0%

The optimised curve (blue) follows the experimental curve (black) closely until it fails. However, after the test specimen reaches the failure strain, the stress does not drop immediately. This is because of the method followed to use force data from post processor to calculate stress. The specimen actually breaks at that point, so it is not a problem within the material model. Table 5.6 shows the error between experimental and simulation test result for tensile test case.

5.2.2 Compression test simulation

Optimised result for compression test with **MAT_124* and **MAT_124 + *MAT_ADD_EROSION* material card is shown in Figure 5.6. The optimised parameters related to compression test along with lower and higher bounds used in Ls-Opt is shown in Table 5.7.

Table 5.7: Setup and results for compression-related variables in **MAT_124* and **MAT_ADD_EROSION*.

	Lower bound	Baseline model	Upper bound	Optimal value
EC	9800	9800	13000	9800.06
PC	34	34	38	35.8134
CC1	0.0088	0.0088	0.0125	0.010082
CF1	0.009	0.009	0.035	0.011326

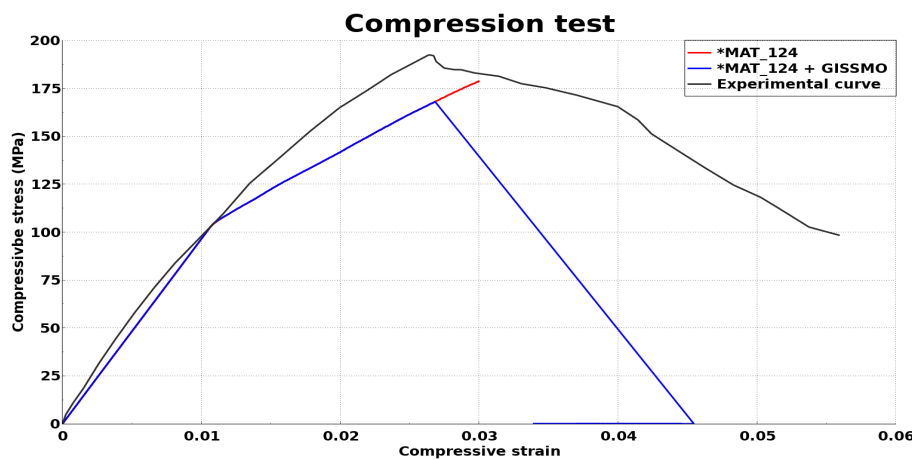

Figure 5.6: Compression test simulation results using **MAT_124* and GISSMO.

Table 5.8: Error calculation in compression test simulation.

Compression test	Experimental value	optimisation value	Error
Failure stress (MPa)	192.64	168.421	14.38%
Failure strain	0.0266	0.0267	0.03%

The optimised curve (blue) does not follow the experimental curve (black) up to maximum stress. The optimised result also depends on the hardening curve shown in Figure 4.11. As the hardening curves were not optimised in this thesis framework, the optimised curve under-predicts maximum stress reached by the material and it could be also because of the material cards limitation for CSM materials as **MAT_124* is built on Von Mises yield surface. Table 5.8 shows the error between experimental and simulation test result for compression test case.

5.2.3 Shear test simulation

Optimised result for shear test with **MAT_124* and **MAT_124 + *MAT_ADD_EROSION* material card is shown in Figure 5.7. The optimised parameters related to shear test along with lower and higher bounds used in Ls-Opt is shown in Table 5.9.

Table 5.9: Setup and results for shear-related variables in **MAT_ADD_EROSION*.

	Lower bound	Baseline model	Upper bound	Optimal value
SC1	0.0046	0.0046	0.008	0.00746069
SF1	0.008	0.008	0.01	0.00869916

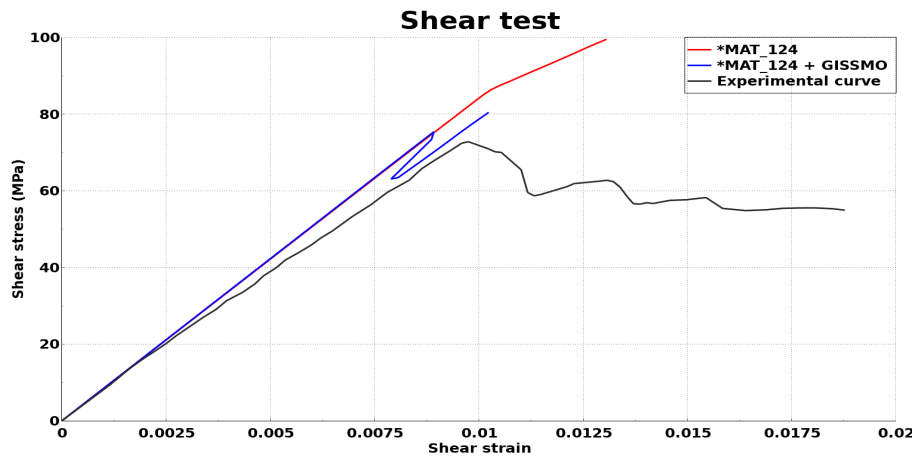
**Figure 5.7:** Shear test simulation results using **MAT_124* and GISSMO.

Table 5.10: Error calculation in shear test simulation.

Shear test	Experimental value	optimisation value	Error
Failure stress (MPa)	73.6	75	1.9%
Failure strain	0.0096	0.0089	7.8%

The optimised curve (blue) is stiffer and over predicts the strength compared to the experimental curve (black). This could be because of the hardening curve it follows during the simulation. Also there is no dedicated parameters to control shear behaviour in either **MAT_124* or **MAT_ADD_EROSION*. Once again this could be one of the limitation of material card **MAT_124* for CSM materials. Table 5.10 shows the error between experimental and simulation test result for shear test case.

5.2.4 Flexural test simulation

Optimised result for flexural test with **MAT_124* and **MAT_124 + *MAT_ADD_EROSION* material card is shown in Figure 5.8. The optimised parameters related to shear test along with lower and higher bounds used in Ls-Opt is shown in Table 5.11.

Table 5.11: Setup and results for flexural-related variables in **MAT_ADD_EROSION*.

	Lower bound	Baseline model	Upper bound	Optimal value
FC1	0.0068	0.0068	0.024	0.00837531
FF1	0.025	0.025	0.04	0.0351355

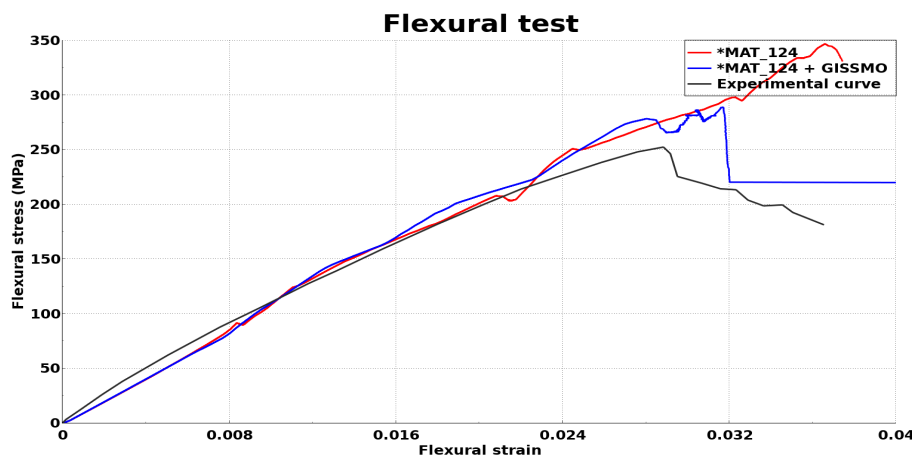
**Figure 5.8:** Flexural test simulation results using **MAT_124* and GISSMO.

Table 5.12: Error calculation in flexural test simulation.

Flexural test	Experimental value	optimisation value	Error
Failure stress (MPa)	251.5	288.235	14.6%
Failure strain	0.029	0.0318	9.6%

The optimised curve (blue) does not follow the experimental curve (black) quite well and after the material reaches 200 MPa it gets overly stiff. There was a lack of information in the physical coupon test report about the co-efficient of friction between the test specimen, support and punch. It did not provide information about the load span as well and also the hardening curve was not optimised in this thesis. So all these factors affected the flexural test result. Table 5.12 shows the error between experimental and simulation test result for flexural test case.

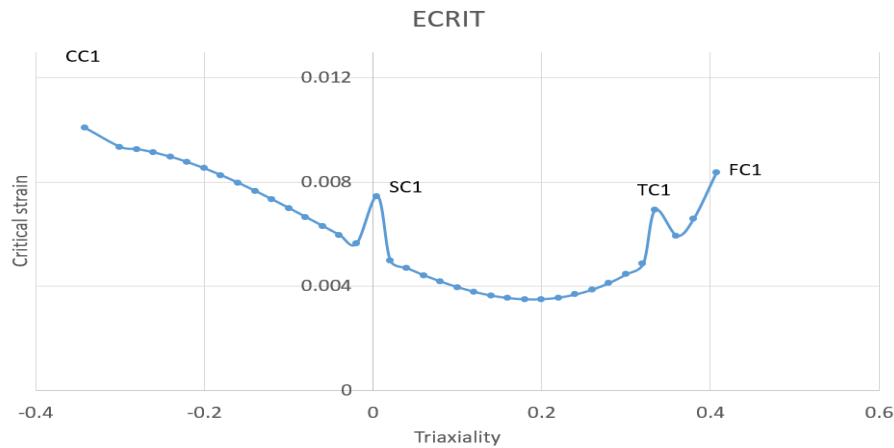
Other parameters

The optimised parameters that effects all test is shown in Table 5.13 along with the lower and higher bounds used in Ls-Opt.

Table 5.13: Setup and results for variables in **MAT_124* and **MAT_ADD_EROSION*.

	Lower bound	Baseline model	Upper bound	Optimal value
DMGEXP	2	2	8	7.39548
FADEXP	2	2	8	7.77847
RPCT	RPCT= PT/PC			0.497645
PR	0.21	0.21	0.23	0.21

The optimised ECRIT and LCSDG curve is as shown in Figure 5.9 and 5.10. Smooth triaxiality curve was not achieved because of time constraint.

**Figure 5.9:** Critical strain vs triaxiality curve after optimisation (ECRIT).

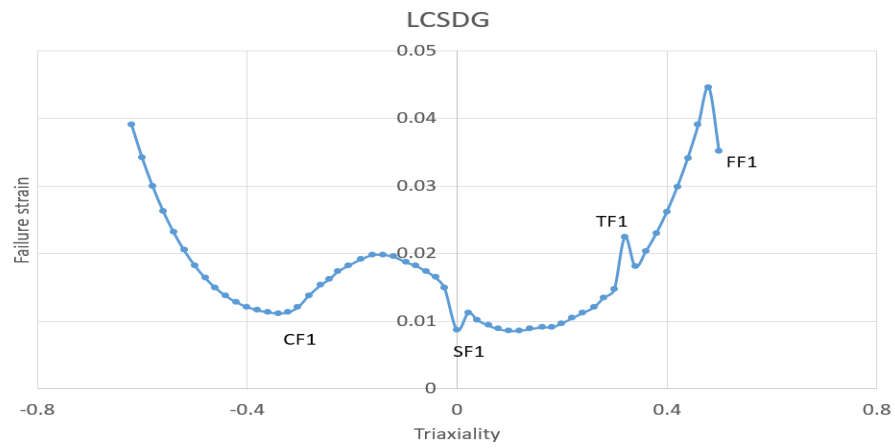


Figure 5.10: Failure strain vs triaxiality curve after optimisation (LCSDG).

6

Conclusion and Future work

6.1 Concluding remarks

In this thesis framework, two material models(**MAT_058* and **MAT_124*) available in LS-DYNA were used for characterising the material behaviour of CSM and the matrix. Both the material models were described along with the input data available from the experimental report. The following conclusion can be made regarding the optimised material models.

- Optimised **MAT_058* material model is in good agreement with the experimental curve in tension, compression and shear tests and it gives a conservative prediction. But the material model could not capture the maximum flexural stress. There was a lack of data in the test report when it comes to bending test and there was no dedicated parameter meant for bending in the **MAT_058* material model. So these two factors affected the bending simulation. Overall it can be concluded that the optimised **MAT_058* material model meets the objective of this thesis.
- Optimised **MAT_124* material model is in good agreement with the experimental curve for tension and compression tests. But it could not capture shear and bending behaviour as it overestimates the actual test results. **MAT_124* material model is built on von Mises yield surface and CSM material might not follow von Mises yield surface so, **MAT_124* may not be the right material model to characterise the behaviour of CSM materials. Another reason for this behaviour could be because that the hardening curves were not optimised and there was no dedicated parameter for controlling shear and bending behaviour in the **MAT_124* material model. So optimised **MAT_124* material model does not meet the objective of this thesis completely.

6.2 Future work

For **MAT_058* material model all the required material data was available from the test report, but for **MAT_124* there were few data missing in the test report. As mentioned earlier, physical test was performed prior to this thesis work. For optimising the *GISSMO* damage model, additional experimental testing (e.g. shear 0°, shear 15°, shear 30°, shear 45°, notched R1 and Bi-axial test) should be performed to calibrate the model parameters to better be able to judge the predictability of

**MAT_124* material model.

The ASTM D6641/D6641M-09 standard followed for the compression test in the provided test report would not give accurate compression modulus value. So it would be good to test the material using ASTM D695 or ISO 604 standard for conducting compression tests.

There are other advanced composite material models in LS-DYNA such as **MAT_158*, **MAT_215* and **MAT_262* which could be investigated in future because they support modelling short fibre composites. Strain rate dependency and mesh regularisation needs to be investigated to get a more complete and versatile material model in the future.

Bibliography

- [1] J. V. Rosen, "*Simulating fracture of laminated glass windscreens undergoing large deformations*", KTH Royal Institute of Technology School of Engineering Sciences, 2018.
- [2] P. Mallick, "*Failure of polymer matrix composites (PMCs) in automotive and transportation applications*", Failure Mechanisms in Polymer Matrix Composites, 2012.
- [3] "*LS-DYNA Keyword User's Manual - Volume I, Version R 11.0*", Livermore Software Technology Corporation, 2018.
- [4] "*Glasspar G2*", Wikipedia.
- [5] B. D. Agarwal, L. J. Broutman, and K. Chandrashekhra, "*Analysis and Performance of Fiber Composites*". John Wiley, 2006.
- [6] G. Slayter, "*Method and apparatus for making glass wool*", US Patent, 1937.
- [7] T. P. Sathishkumar, S. Satheeshkumar, and N. Jesuarockiam, "*Glass fiber-reinforced polymer composites – a review*", Journal of Reinforced Plastics and Composites, 2014.
- [8] S. S. Heckadka, S. Y. Nayak, K. Narang, and K. V. Pant, "*Chopped Strand/- Plain Weave E-Glass as Reinforcement in Vacuum Bagged Epoxy Composites*", Journal of Materials, Hindawi Publishing Corporation, 2015.
- [9] W. Cantwell and S. Youd, "*Rate effects in the fracture of glass fibre chopped strand mat composites*", Composites Part B: Engineering, 1997.
- [10] S. Y. Nayak, S. S. Heckadka, L. G. Thomas, and A. Baby, "*Tensile and Flexural Properties of Chopped Strand E-glass Fibre Mat Reinforced CNSL-Epoxy Composites*", Materials Science and Engineering, 2018.
- [11] British Standards Institution, 1973.
- [12] S. Zhang, P. D. Soden, and P. M. Soden, "*Interlaminar shear fracture of chopped strand mat glass fibre reinforced polyester laminates*", Composites, 1986.
- [13] M. Johar, K. O. Low, H. A. Israr, and K. J. Wong, "*Mode I and mode II delamination of a chopped strand mat E-glass reinforced vinyl ester composite*", Plastics Rubber and Composites, 2018.
- [14] A. M. T. Arifin, S. Abdullah, M. Rafiquzzaman, R. Zulkifli, D. A. Wahab, and A. Arifin, "*Investigation of the behaviour of a chopped strand mat/woven roving/ foam-Klegecell composite lamination structure during Charpy testing*", Materials Design, 2014.
- [15] B. P. Naughton, F. Panhuizen, and A. C. Vermeulen, "*The Elastic Properties of Chopped Strand Mat and Woven Roving in G.R. Laminae*", Journal of Reinforced Plastics and Composites, 1985.

- [16] M. J. Owen and R. Dukes, "*Failure of glass-reinforced plastics under single and repeated loading*", Journal of Strain Analysis, 1967.
- [17] V. Monfared, "*31 - Problems in short-fiber composites and analysis of chopped fiber-reinforced materials*", New Materials in Civil Engineering, 2020.
- [18] J. F. Mandell, "*Fatigue behavior of short fiber composite materials*", Composite materials series, 1991.
- [19] "*LS-DYNA theory manual, r:11261*", Livermore Software Technology Corporation, 2019.
- [20] A. Matzenmiller, J. Lubliner, and R. L. Taylor, "*A constitutive model for anisotropic damage in fiber-composites*", Mechanics of Materials, 1995.
- [21] K. Schweizerhof, K. Weimar, T. Münz, and T. Rottner, "*Crashworthiness analysis with enhanced composite material models in LS-DYNA- Merits and Limits*", LS-DYNA World Conference, 1998.
- [22] "*LS-DYNA Keyword User's Manual - Volume II. Material Models, Version R 11.0*", Livermore Software Technology Corporation, 2018.
- [23] D. J, "*Notes on composite model*", [Online]. Available: <https://ftp.lstc.com/anonymous/outgoing/jday/faq/composite.models>.
- [24] C. Goyal, "*Uncertainty Quantification in Non-linear Seismic Wave Propagation*", Carleton University, 2017.
- [25] P. Reithofer, A. Fertschej, B. Hirschmann, B. Jilka, and M. Rollant, "*Material Models For Thermoplastics In LS-DYNA From Deformation To Failure*", 15th International LS-DYNA Users Conference, 2018.
- [26] J. Lemaitre, "*A Continuous Damage Mechanics Model for Ductile Fracture*", Journal of Engineering Materials and Technology, 1985.
- [27] S. Charoenphan, L. C. Bank, and M. E. Plesha, "*Use of LS-DYNA shell elements in the analysis of composite plates with unbalanced and unsymmetric layups*", Use of LS-DYNA shell elements in the analysis of composite plates with unbalanced and unsymmetric layups, 2000.
- [28] A. Shahkarami and R. Vaziri, "*A continuum shell finite element model for impact simulation of woven fabrics*", International Journal of Impact Engineering, 2007.
- [29] N. Stander and K. J. Craig, "*Response surface and sensitivity based optimization in Ls-Opt: A benchmark study*", 7th International LS-DYNA Users Conference, 2002.
- [30] D. J. Benson, N. Stander, M. R. Jensen, and K. J. Craig, "*On the application of Ls-Opt identify non-linear material models in LS-DYNA*", 7th International LS-DYNA Users Conference, 2002.
- [31] H. Müllerschön, U. Franz, T. Münz, and N. Stander, "*The identification of rate-dependent material properties in foams using Ls-Opt*", Livermore Software Technology Corporation, 2001.
- [32] S. Dong and K. S. Carney, "*Modeling of Carbon-Fiber-Reinforced-Polymer(CFRP) Composites in Ls-Dyna with optimization of material and failure parameters in Ls-Opt*", 15th International LS-DYNA Users Conference, 2018.
- [33] "*ISO8256 Plastics — Determination of tensile-impact strength*", International Organization for Standardization, 2004-07.

-
- [34] *"D638-14 Standard Test Method for Tensile Properties of Plastics"*, American Society for Testing and Materials, 2015.
 - [35] *"DatapointLabs tensile test specimen for ISO 8256 standard"*, DatapointLabs, 2014.
 - [36] *"D6641M16 Standard Test Method for Compressive Properties of Polymer Matrix Composite Materials Using a Combined Loading Compression (CLC) Test Fixture1"*, American Society for Testing and Materials, 2016.
 - [37] *"D5379/D5379M-12 Standard Test Method for Shear Properties of Composite Materials by the V-Notched Beam Method"*, American Society for Testing and Materials, 2013.
 - [38] *"DatapointLabs Iosipescu specimen for ASTM D5379 standard"*, DatapointLabs, 2014. [Online]. Available: https://www.datapointlabs.com/images/Specimens/Iosipescu_specimen.pdf.
 - [39] *"D6272-17 Standard Test Method for Flexural Properties of Unreinforced and Reinforced Plastics and Electrical Insulating Materials by Four-Point Bending"*, American Society for Testing and Materials, 2017.
 - [40] *"ASTM D792-13 Standard Test Methods for Density and Specific Gravity (Relative Density) of Plastics by Displacement"*, American Society for Testing and Materials, 2013.
 - [41] *"Consistent units"*, LS-DYNA Support.
 - [42] M. Klasztorny, A. Bondyra, P. Szurgott, and D. Nycz, *"Numerical modelling of GFRP laminates with MSC.Marc system and experimental validation"*, Computational Materials Science, 2012.
 - [43] D. J., *"Notes on *MAT_058"*, [Online]. Available: https://ftp.lstc.com/anonymous/outgoing/support/FAQ_kw/composites/mat58.
 - [44] D. M. Nuruzzamana, M. A. Chowdhury, M. M. Rahman, M. A. Kowser, and B. K. Roy, *"Experimental investigation on friction coefficient of composite materials sliding against SS 201 and SS 301 counterfaces"*, 6th BSME International Conference on Thermal Engineering, 2014.
 - [45] Y. Liu and G. Glass, *"Effects of Mesh Density on Finite Element Analysis"*, SAE, 2013.
 - [46] S. Kut, *"State of stress identification in numerical modeling of 3D issues"*, Archives of Metallurgy and Materials, 2009.
 - [47] J. Koyanagi and M. Sato, *"Time and temperature dependence of transverse tensile failure of unidirectional carbon fiber-reinforced polymer matrix composites"*, Creep and Fatigue in Polymer Matrix Composites (Second Edition), 2019.
 - [48] S. Olufsen, A. H. Clausen, and O. S. Hopperstad, *"Influence of stress triaxiality and strain rate on stress-strain behaviour and dilation of mineral-filled PVC"*, Polymer Testing, 2019.

